臺灣地區 110 年中大型地震震源資訊之快速彙整與提供

子計畫一

中大規模地震震源破裂特性近即時分析

李憲忠 劉庭佑

中華民國地球物理學會

Part 1.

Preliminary result of the source rupture process of April 18, 2021 M_L6.2 Hualien earthquake

1.1 Introduction

On April 18, 2021, a big earthquake struck eastern Taiwan. This earthquake had a local magnitude M_L6.2, and the epicenter (121.48, 23.86) was located in a mountain area of about 20 km southwest of Hualien city with a depth of approximately 13.9 km (Figure 1.1). The ground-shaking near the source area was extremely large, the largest intensity was observed in the Shuilian, Hualien county, with a maximum intensity 6 (>250 gal) on the Central Weather Bureau intensity scale. Large felt intensity (intensity 4, >25 gal) extended toward most of western Taiwan. Strong ground shaking was also observed in Taipei city with intensity 3. Fortunately, no people have died during this event.

The 2021 Hualien earthquake occurred in a complex tectonic area. It is located on the western side of the northern Longitudinal Valley, which is a suture zone of the Eurasian Plate and Philippine Sea Plate. The Ryukyu trench is located on the eastern side where the Philippine Sea Plate is subducted beneath the Eurasian Plate. Thousands of earthquakes occurred in this junction area every year. During the time period from October to December in 1951, three big events with a magnitude larger than M7 and thousands of aftershocks occurred between Hualien and Taitung along the Longitudinal Valley. This earthquake series is known as the Longitudinal Valley Earthquake sequence. It is also noted that the hypocenter of this event was very close to the Mw 6.4 Hualien earthquake that occurred in 2019. Due to its similarity in both magnitude and epicenter location, people are worried about the possibility of followed by big events. In this preliminary study, I perform a joint source inversion by using teleseismic and local seismograms to analyze the rupture process and try to realize how the extremely strong ground shaking occurred at Shuilian.

1.2 Data and Method

The joint inversion waveform data were taken from IRIS GSN stations and two local seismic networks, including the BATS and CWB 24-bit Seismic Monitoring Network (CWB24). The displacement P teleseismic waveforms start from 10 seconds before P and 30 seconds after P arrival was used in the inversion. For the local waveform, a 60 second time window beginning from the event origin time was used in the inversion. The band-pass filter range of teleseismic waveforms was 0.01 − 0.33 Hz, and the band-pass filter range of local seismic waveforms was 0.05 − 0.33 Hz for both BATS and CWB24.

The finite fault source inversion problem is generally formulated in a linear form, $\boldsymbol{Ax} = \boldsymbol{b}$ (Hartzell and Heaton, 1983), where $\boldsymbol{A}$ is the matrix of Green's functions, $\boldsymbol{b}$ is the observed data vector, and $\boldsymbol{x}$ is the solution vector of the slip. This inversion problem is solved by using a parallel non-negative least square (Parallel NNLS, Lee et al., 2006). A misfit function, defined as $(\boldsymbol{Ax}-\boldsymbol{b})^2 / \boldsymbol{b}^2$, was used to evaluate the fit of the data. The multiple-time window was considered in this inversion. There were 16 time-windows, each having 0.4 second duration and overlapping 0.2 second. In matrix A, the local 3D synthetic Green's functions were calculated based on the spectral-element method (SEM, Komatitsch et al., 1999). The teleseismic Green's functions were calculated by the IRIS Synthetics Engine (Syngine; IRIS DMC, 2015) for the 1D Earth reference model using the Preliminary Reference Earth Model (PREM, Dziewonski and Anderson, 1981). Both the teleseismic and local synthetic Green's functions were filtered to the same frequency bands applied to the observed data.

Two fault planes based on the focal mechanism reported by the RMT were considered in this study (Figure 1.1). One with a nearly N-S strike, dipping to the west (strike 199°, dip 52°, Fault 1), and the other is a nodal plane with a NE-SW strike, dipping to the east (strike 70°, dip 50°, Fault 2). The two fault planes were divided into 264 subfaults and each with a size of 9 km^2. The rupture speed was allowed to vary between 0.0 and 4.0 km/s in the inversion. Because the inversion result of NE-SW strike nodal fault plane (Fault 2) was worse than the other fault plane, the report was focused on the inversion results on Fault 1 in the following discussions. The data fittings of Fault 1 are shown in Figure 1.2 and Figure 1.3.

1.3 Inversion result

Slip distribution

The source inversion result of 2021 Hualien earthquake shows a concentrated slip pattern (Figure 1.4 and Figure 1.5). Only one large asperity was found on the fault plane. The slip near the hypocenter was large of about 20 cm which shows a nearly thrust movement. The maximum slip was 22.7 cm located close to the epicenter. The slip at asperity was mainly thrust and gradually had a more strike-slip component to the south. Note that this slip concentrated area was located in the middle depths of the fault plane (10-15 km depth). No obvious slip occurred in the shallower fault plane of less than 10 km depth. This implies that the rupture of this event was not extended to the shallow crust, and thus without surface break observed. It is also noted that both the foreshock and mainshock centroid reported by RMT (red open circle in Figure 1.4 and Figure 1.5)

were located close to the CWB mainshock hypocenter. The slip zone and aftershock distribution both show a northeast to southwest trend (Figure 1.4). Most of the big aftershocks were located around the main slip zone (Figure 1.5). The average slip on the fault plane is about 11.2 cm.

Rupture process

The accumulated slip snapshot is shown in Figure 1.6. The initial slip was strong near the hypocenter. After that, the rupture quickly propagated bilaterally. The rupture mainly occurred on the middle fault plane that produced a large asperity from 1 to 8 seconds. The slip also extended to the southern fault plane at about 10-12 seconds after the initial rupture which finally formed a southern slip pattern.

Three reference rupture fronts with constant rupture velocities are shown in Figure 1.6. They are Vr=4.0km/s, 3.0km/s and 2.0km/s, respectively. The rupture propagated was generally lied in between the 3.0 km/s and 2.0 km/s rupture fronts. This implied that the maximum rupture speed of this event was about 3.0 km/s.

A two peaks seismic moment release history can be found from the moment rate function (Figure 1.7). The first moment releases occurred at 1-8 seconds, this was caused by the initial slip and subsequent bilateral rupture process. During this time period, the moment release is related to the developments of asperity. The secondary moment release can be observed between 10 and 14 seconds that was related to a small slip that occurred in the southern area before the end of the rupture. The entire duration time of this event is about 15 seconds, with two peaks at approximately 4 and 11 seconds. The total seismic moment is about 1.47×10^{19} Nm, which is equivalent to an Mw 6.04 earthquake.

1.4 Forward ground motion simulation

In order to know how the extremely strong ground shaking occurred in the Hualien county, an island-wide three-dimensional ground motion simulation was performed using the spectral-element method (Komatitsch et al., 2004; Lee et al., 2008). A comparison between the observed intensity map and synthetic peak ground acceleration maps (finite-fault and point double-couple source) is shown in Figure 1.8. Most of the observed intensity characteristics could be reproduced by the simulation. Large PGA were occurred in east and central Taiwan, including Hualien and Taichung. Weaker PGAs were observed in most of southern and northern Taiwan. These phenomena were reproduced by the synthetic PGA (Figure 1.8b). An extremely large PGA (723.59 gal) was observed at the eastern side of the epicenter, close to Shuilian (Figure 1.8a). The synthetic PGA can reproduce this phenomenon. This extremely large PGA was also observed in the simulation result of point double-couple source (Figure 1.8c). It implies that this phenomenon was mainly caused by the source radiation pattern rather than the rupture directivity.

References

Dziewonski, A. M. and D. L. Anderson (1981). Preliminary reference Earth model (PDF), *Physics of the Earth and Planetary Interiors*, 25(4) 297–356.

Hartzell, S. H., Heaton, T. H. (1983). Inversion of strong ground motion and teleseismic waveform data for the fault rupture history of the 1979 Imperial Valley, California earthquake. *Bulletin of the Seismological Society of America*, 73, 1553–1583.

IRIS DMC (2015). Data Services Products: Synthetics Engine, https://doi.org/10.17611/DP/SYNGINE.1.

Komatitsch, D., Tromp, J. (1999). Introduction to the spectral-element method for 3-D seismic wave propagation. *Geophysical Journal International*, 139, 806-822.

Lee, S. J., H. W. Chen, Q. Liu, D. Komatitsch, B. S. Huang, and J. Tromp (2008). Three dimensional simulations of seismic wave propagation in the Taipei basin with realistic topography based upon the spectral-element method, *Bull. Seismol. Soc. Am.* 98 253–264. http://dx.doi.org/10.1785/0120070033.

Lee, S. J., Ma, K. F., Chen, H. W. (2006). Three-dimensional dense strong motion waveform inversion for the rupture process of the 1999 Chi-Chi, Taiwan, earthquake. *J. Geophys. Res.: Solid Earth* (1978–2012) 111, B11.

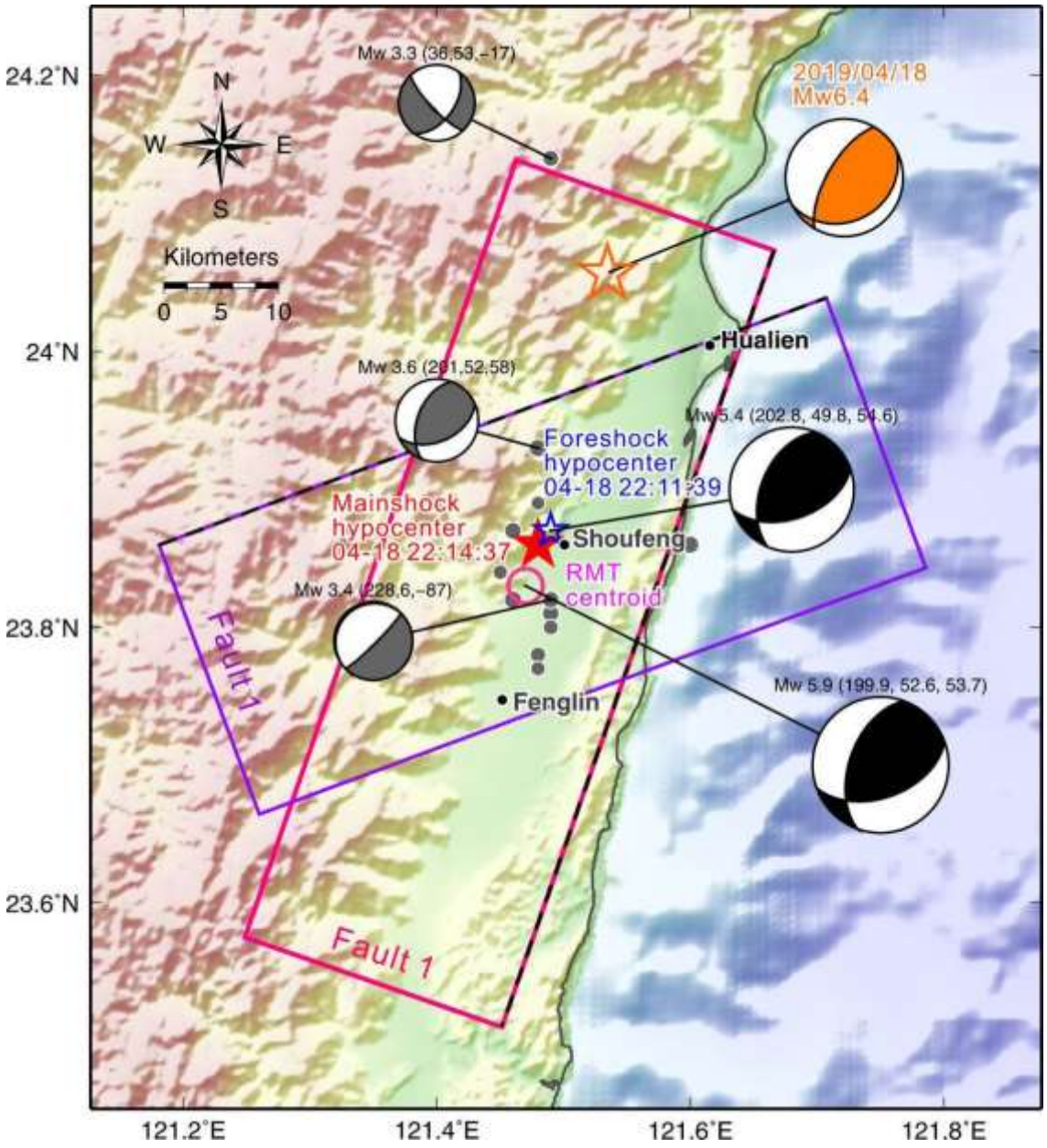

Figure 1.1 The location map of the 2021 M_L6.2 Hualien earthquake. The red star indicates the CWB epicenter of this event and the pink open circle represents its centroid determined by RMT. Aftershocks occurred within two weeks after the mainshock is shown by the gray circles. The epicenters of foreshock and 2019 Hualien earthquake are shown by the blue and orange open stars, respectively. Pink and purple open rectangles indicate the two fault planes (Fault 1, Fault 2) taken from RMT focal mechanism. Their shallowest portions are shown by dotted lines.

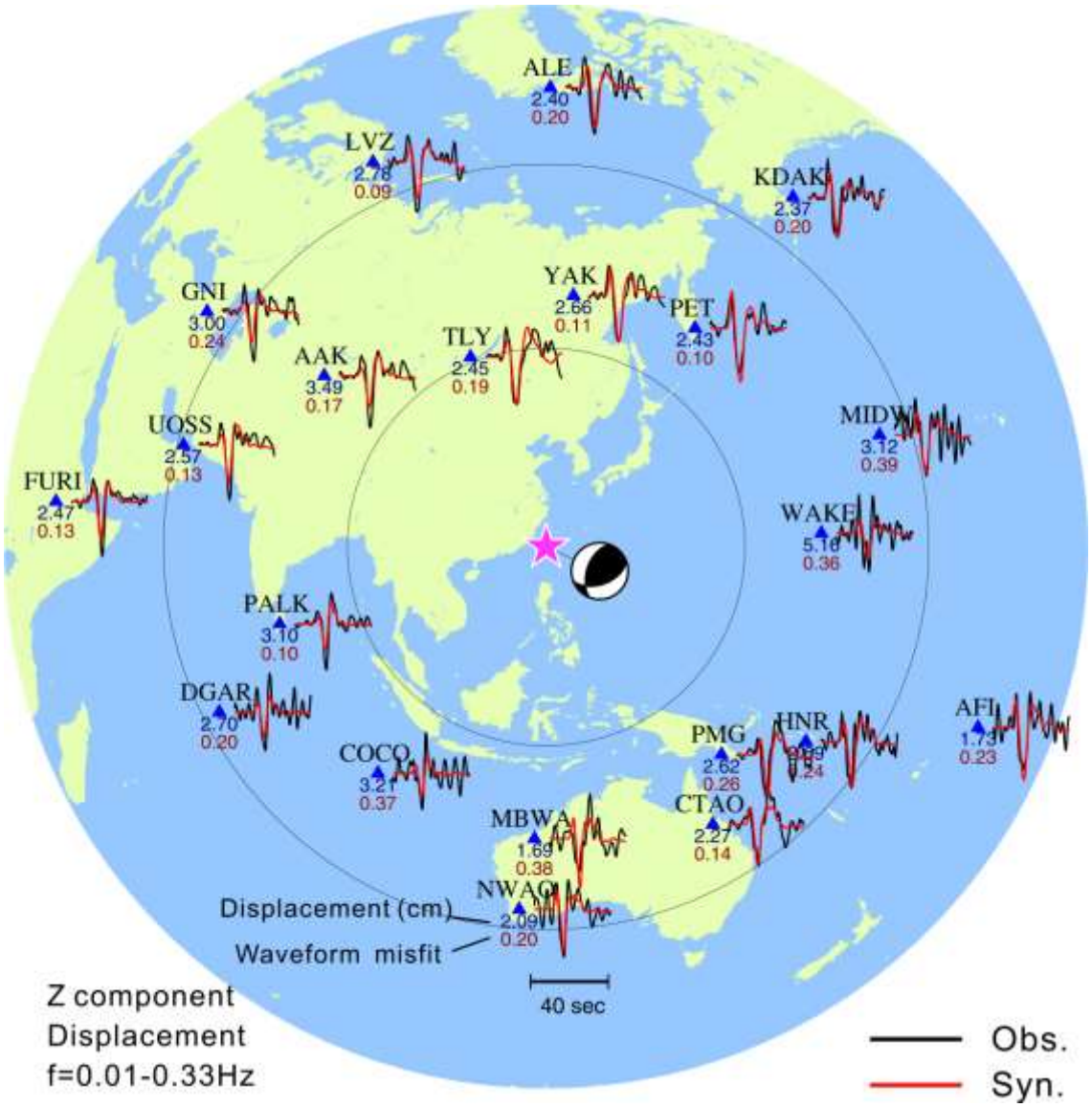

Figure 1.2 Comparison between the observed and synthetic teleseismic P wave displacement waveforms. The black lines denote the observations, and the red lines represent the synthetics. The IRIS GSN waveforms are band-pass filtered between 0.01 and 0.33 Hz. A 40 seconds time window starts from 10 seconds before P and 30 seconds after P arrival was used in the inversion. The maximum amplitude of the observation (blue number) and waveform misfit (red number), defined as $(Ax\text{-}b)^2/b^2$, are shown at each station.

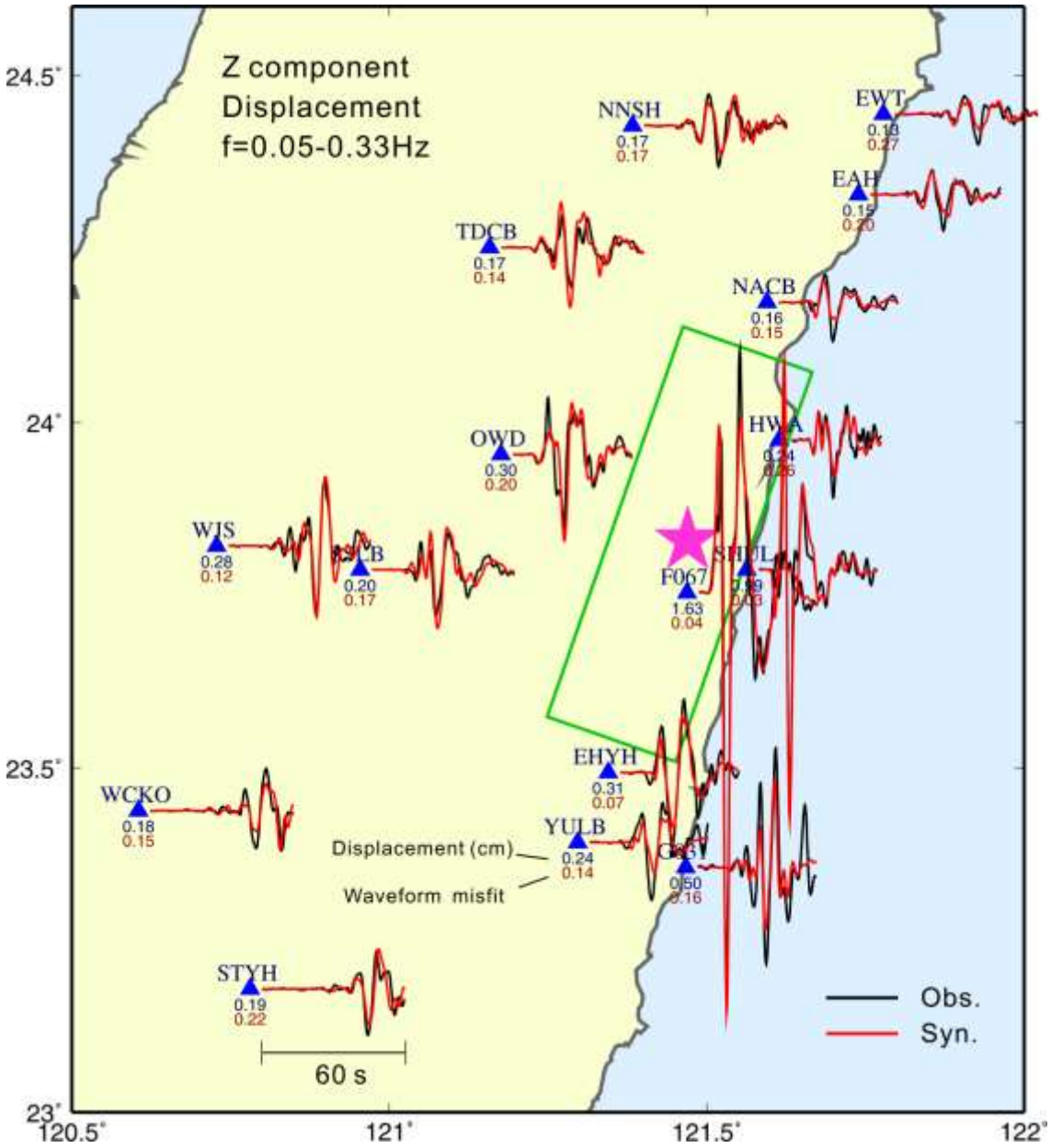

Figure 1.3 Comparison between local observation and synthetic waveforms in the vertical component. The black lines are BATS and CWB 24-bit observations, and the red lines are synthetic waveforms. All the waveforms are in the type of displacement and a band-pass filter with the period between 3 and 20 seconds was applied. The maximum amplitude of the observed displacement waveform and misfit between observation and synthetic are shown at each station. The pink star and green open rectangular are the epicenter and the fault plane projected to the surface, respectively.

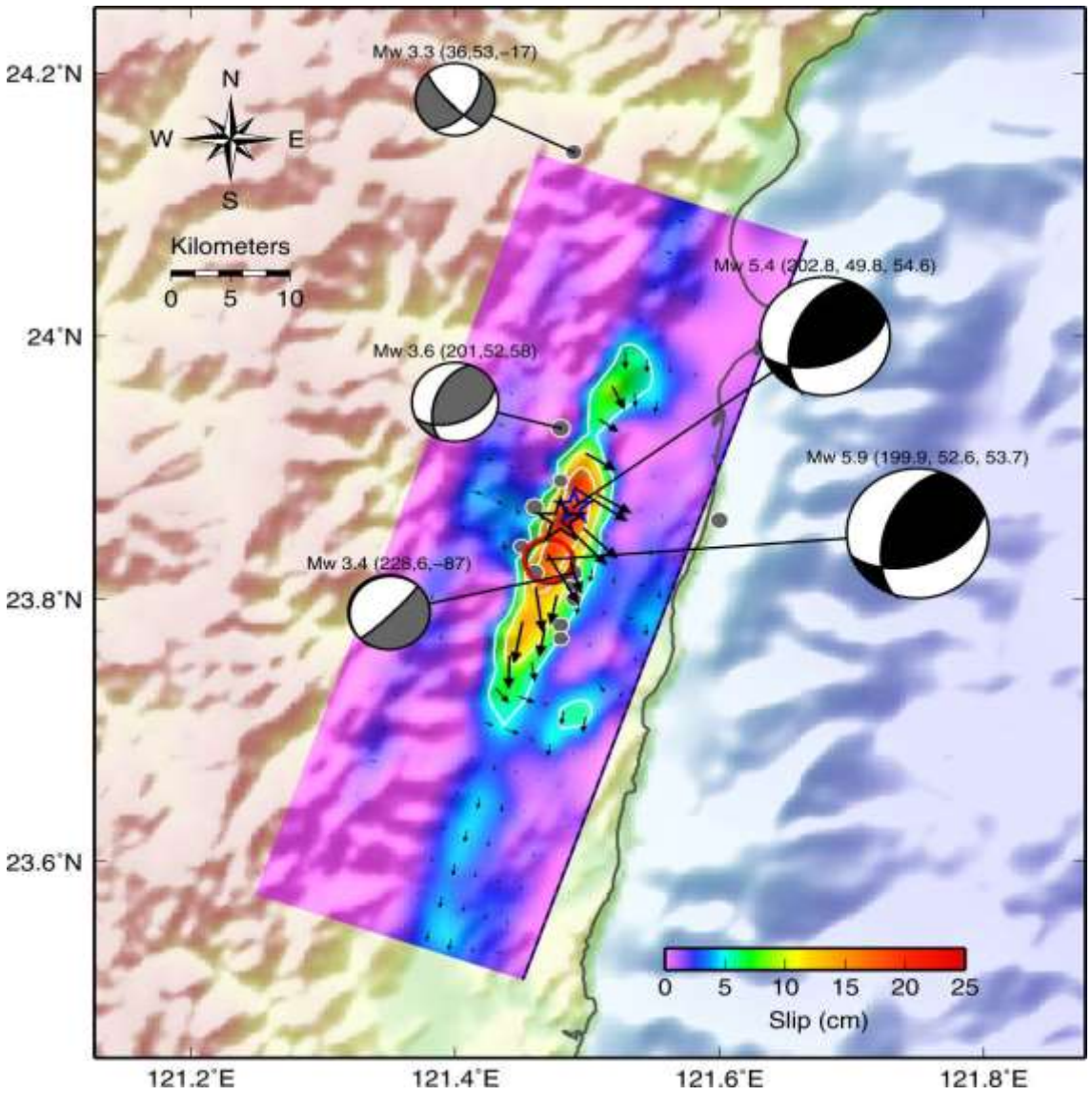

Figure 1.4 The map view of slip distribution of the 2021/04/18 Hualien earthquake. The black open star indicates the epicenter of this event provided by the CWB earthquake report. The red open circle shows the location of the centroid provided by RMT. Gray circles are the two-week aftershocks reported by CWB.

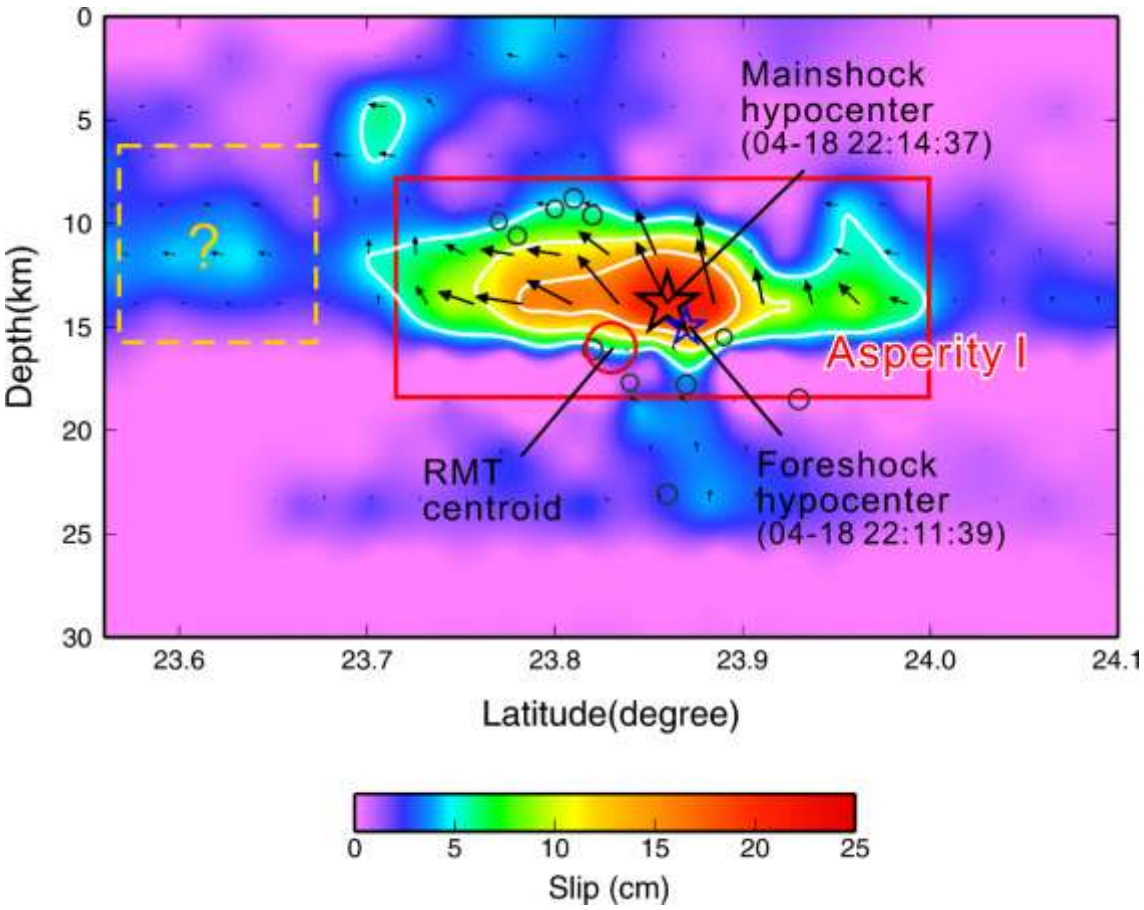

Figure 1.5 Slip distribution on the fault plane. The black open star indicates the epicenter of this event provided by the CWB earthquake report. Red and gray open circle shows the location of centroid provided by RMT and aftershocks, respectively. The red open rectangle presents the area of asperity. The yellow dotted open rectangle indicates the small slip area in the southern fault plane.

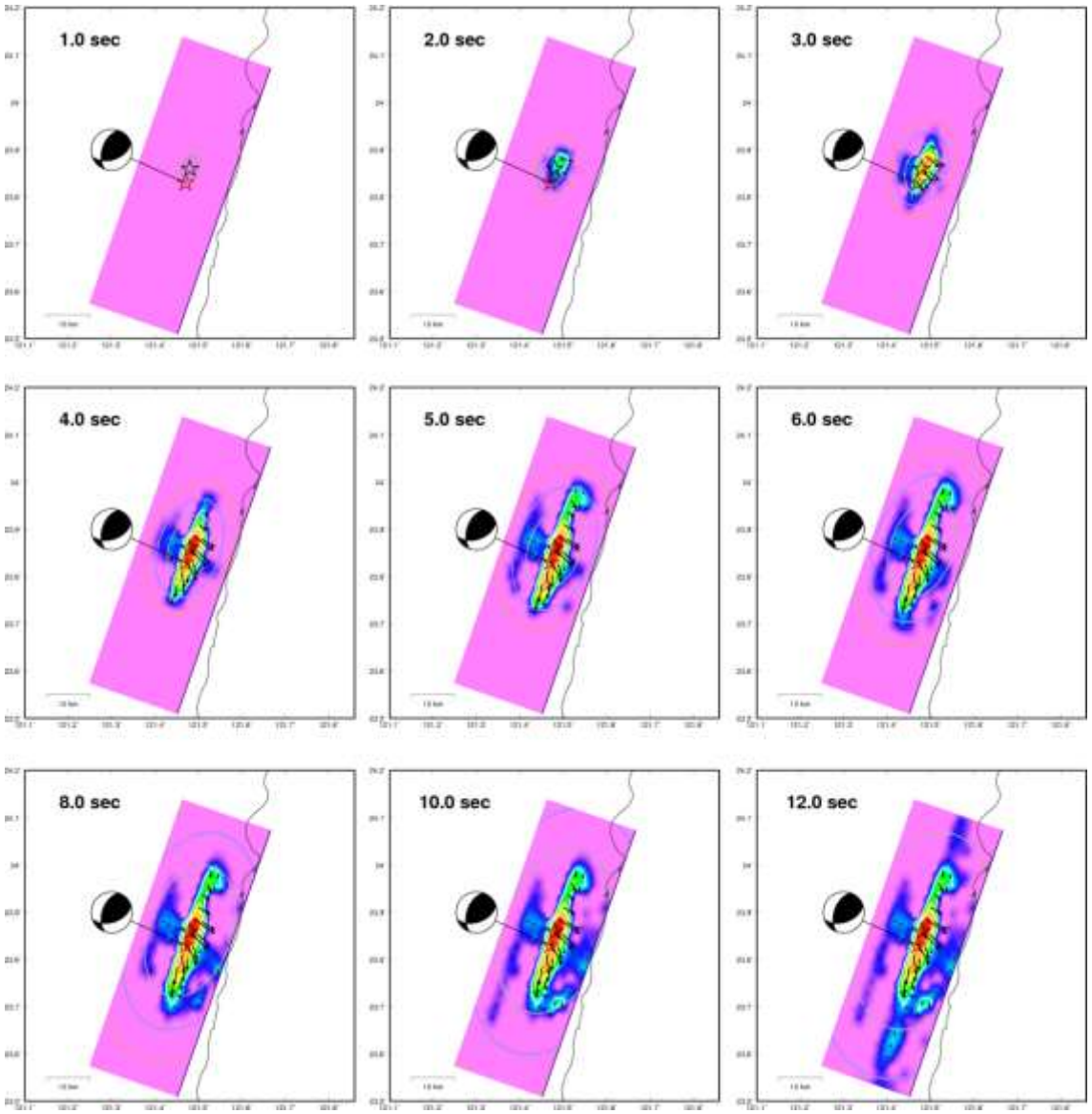

Figure 1.6 Snapshot of cumulative slip. The black open star indicates the hypocenter reported by CWB. The red open star shows the RMT centroid. Three reference rupture fronts with rupture velocity Vr = 4.0 km/s, 3.0 km/s and 2.0 km/s are shown by light-red, light-blue and gray circles, respectively.

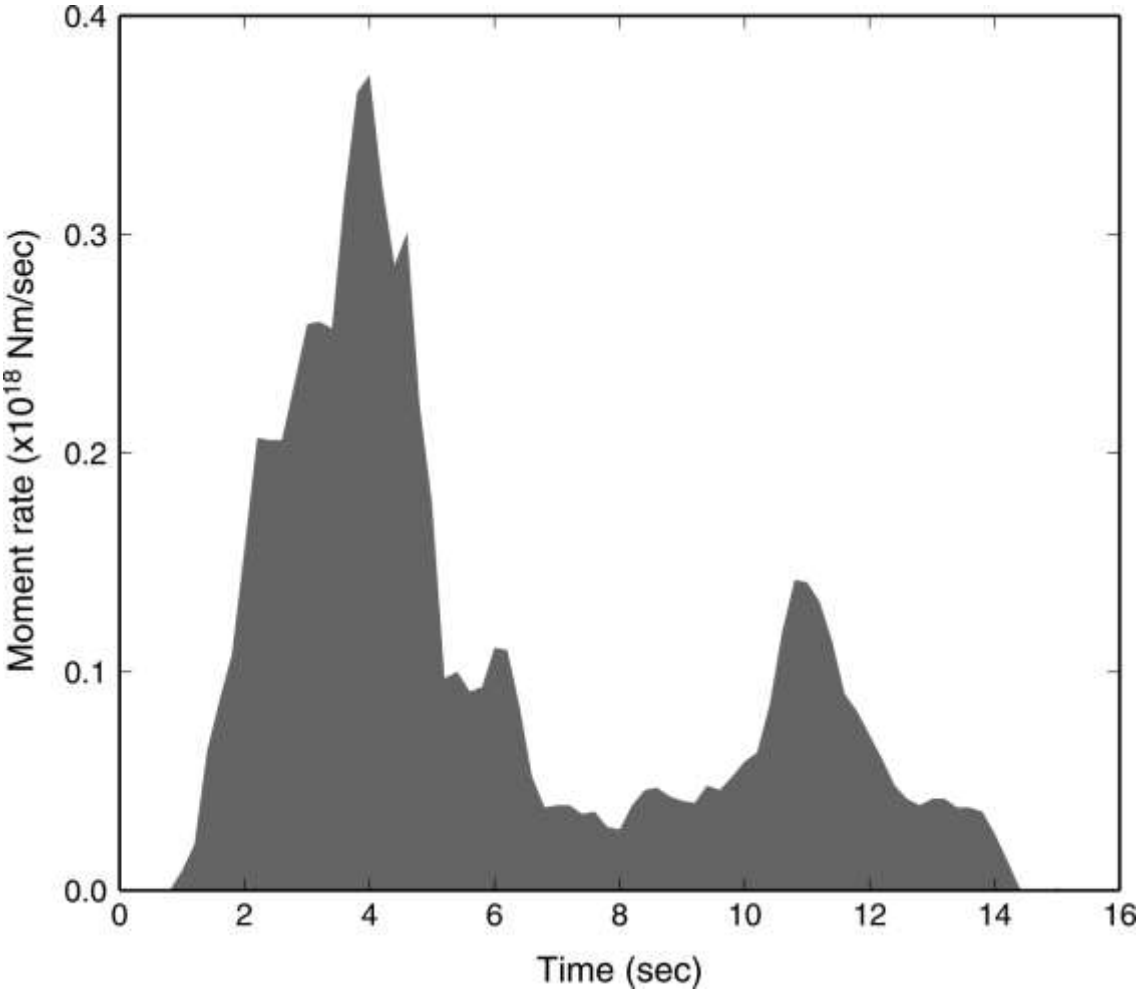

Figure 1.7 The moment rete function of the inversion result.

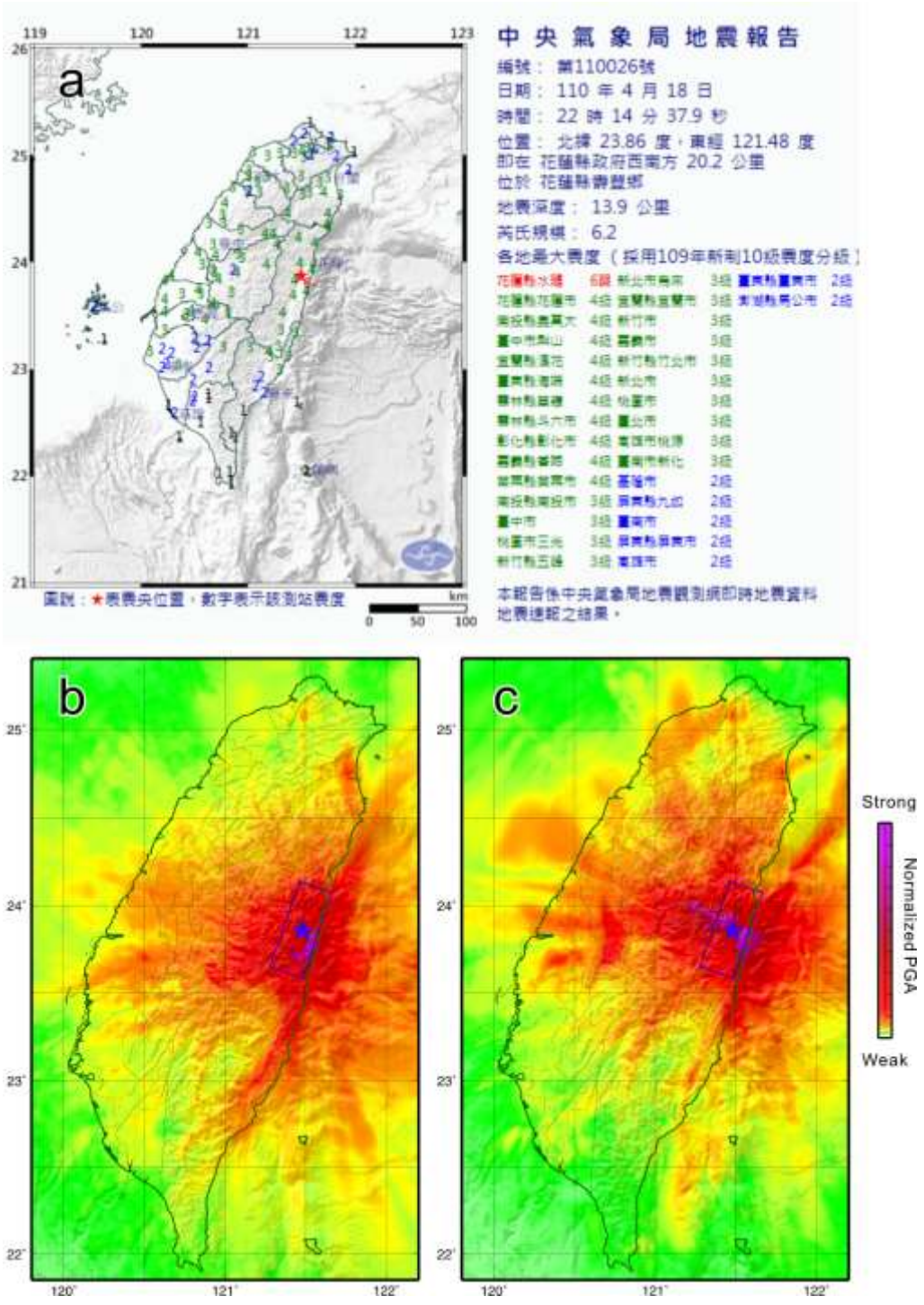

Figure 1.8 (a) Intensity map of the CWB earthquake report. (b) Synthetic PGA distribution derived from the finite-fault rupture model. (c) Synthetic PGA distribution derived from a point double-couple source. The blue star and open rectangular are the epicenter and the fault plane projected to the surface, respectively.

Part 2.

Preliminary result of the joint source inversion of October 24, 2021 M_L6.5 Nanao earthquake

2.1 Introduction

On October 24 2021, a big earthquake struck northern Taiwan. This earthquake had a local magnitude M_L6.5, and the epicenter (121.79, 24.53) was located in a coastal area of about 22.7 km southwest of Yilan county with a depth of approximately 66.8 km (Figure 2.1). The largest intensity was observed in the Yilan county, with a maximum intensity 4 (>25 gal) on the Central Weather Bureau intensity scale. Large felt intensity (intensity 4, >25 gal) extended toward most of northern Taiwan. Strong ground shaking was also observed in Taipei city with intensity 4. Fortunately, no people have died during this event.

The hypocenter depth of the Nanao earthquake is very deep at about 66 km. The geological structure at this depth is not very clear. The most significant structure is the Ryukyu subduction zone on the eastern side where the Philippine Sea Plate is subducted beneath the Eurasian Plate. However, the focal mechanism of this earthquake shows that the two possible fault planes, one NE-SW strike, low angle dipping to the southeast, and the other N-S strike, high angle dipping to the west, do not conform to the subduction zone geometry that dipping to the north/northwest in this area. In this study, a joint source inversion was performed by using teleseismic and local seismograms to analyze the slip distribution and try to realize which could be the true fault plane.

2.2 Data and Method

The joint inversion waveform data were taken from IRIS GSN stations and two local seismic networks, including the BATS and CWB 24-bit Seismic Monitoring Network (CWB24). The displacement P teleseismic waveforms start from 10 seconds before P and 15 seconds after P arrival was used in the inversion. For the local waveform, a 50 second time window beginning from the event origin time was used in the inversion. The band-pass filter range of teleseismic waveforms was 0.01 − 0.5 Hz, and the band-pass filter range of local seismic waveforms was 0.05 − 0.5 Hz for both BATS and CWB24.

The finite fault source inversion problem is generally formulated in a linear form, $\boldsymbol{Ax} = \boldsymbol{b}$ (Hartzell and Heaton, 1983), where $\boldsymbol{A}$ is the matrix of Green's functions, $\boldsymbol{b}$ is the observed data vector, and $\boldsymbol{x}$ is the solution vector of the slip. This inversion problem is solved by using a parallel non-negative least square (Parallel NNLS, Lee et al., 2006). A misfit function, defined as $(\boldsymbol{Ax}-\boldsymbol{b})^2 / \boldsymbol{b}^2$, was used to evaluate the fit of the data. The multiple-time window was considered in this inversion. There were 16 time-windows, each having 0.4 second duration and overlapping 0.2 second. In matrix A, the local 3D synthetic Green's functions were calculated based on the spectral-element method (SEM, Komatitsch et al., 1999). The teleseismic Green's functions were calculated by the IRIS Synthetics Engine (Syngine; IRIS DMC, 2015) for the 1D Earth reference

model using the Preliminary Reference Earth Model (PREM, Dziewonski and Anderson, 1981). Both the teleseismic and local synthetic Green's functions were filtered to the same frequency bands applied to the observed data.

Two fault planes based on the focal mechanism reported by the CWB CMT were considered in this study (Figure 2.1). One fault plane with a NE-SW strike, dipping to the southeast (strike 49°, dip 12°, Fault 1), and the other is a nodal plane with a nearly N-S strike, high-angle dipping to the west (strike 198°, dip 78°, Fault 2). The two fault planes were divided into 323 subfaults and each with a size of 9 km^2. The rupture speed could vary between 0.0 and 4.0 km/s in the inversion. The data fittings of Fault 1 and Fault 2 are shown in Figure 2.2 and Figure 2.3.

2.3 Inversion result

The source inversion result of Fault 1 shows a concentrated slip pattern (Figure 2.1a). Only one large asperity was found on the fault plane. The slip near the hypocenter was large of more than 20 cm which shows a nearly thrust movement. The average slip on the fault plane is about 7.1 cm and the maximum slip was 28.8 cm located close to the epicenter. The slip at asperity was mainly oblique thrust that moved to the northwest. Smaller slips of about 10 cm also extended to a large area northeast of the hypocenter. The total seismic moment is about 2.41×10^{18} Nm, which is equivalent to an Mw 6.18 earthquake. Note that the entire slip area is concentrated in the deep crust approximately 64-69 km. No obvious slip occurred in the shallower fault plane of less than 60 km depth. It is also noted that the mainshock centroid reported by RMT (red open circle in Figure 2.1a), a M_L 5.4 aftershock (blue star), and other aftershocks (gray circles) were located at the western side close to the asperity (Figure 2.1a).

Fault 2 also shows a concentrated slip pattern (Figure 2.1b) with only one large asperity was found on the northern fault plane about 15 km away from the hypocenter. The slip near the hypocenter was smaller of less than 10 cm. The average slip on the fault plane is about 7.3 cm and the maximum slip was 24.1 cm located in the northern area of the fault plane. The total seismic moment is about 2.07×10^{18} Nm, which is equivalent to an Mw 6.14 earthquake. The slip not only ruptured to the north but also extended in the deep crust of approximately 60-80 km depths. Noted that the mainshock centroid reported by RMT (red open circle in Figure 2.1b), the biggest aftershock M_L5.4 (blue star), and other aftershocks (gray circles) were not located in the slip area. (Figure 2.1b).

2.4 Forward ground motion simulation

Island-wide three-dimensional ground motion simulations were performed using the spectral-element method (Komatitsch et al., 2004; Lee et al., 2008). A comparison between the observed intensity map and synthetic peak ground acceleration maps based on the inverted finite-fault source models of Fault 1 and Fault 2 is shown in Figure 2.4. Both the synthetic PGA maps show strong ground shaking in northern Taiwan, including Yilan and Taipei. Weaker PGAs were found in central and southern Taiwan. However, the large PGA pattern of Fault 1 shows a northwest to southeast pattern (Figure 2.4b) which is closer to that in the observed intensity map. This might imply that the radiation pattern of the rupture of Fault 1 can much better explain the observed

shaking pattern.

2.5 Summary

From the above analyses, the finite-fault slip distribution of Fault 1 can have a better explanation for aftershock distribution and centroid location. The synthetic PGA pattern based on Fault 1 also fits better to the observed intensity map. Thus, this preliminary result suggests that the NE-SW strike, low angle dipping to the southeast fault plane (strike 49°, dip 12°, Fault 1) could be the seismogenic structure of this earthquake. Different from the north to northwest dipping subduction interface in this area, the low angle southeast dipping fault plane might be like a conjugate to the lower boundary of the subducting slab. However, more data and analysis are needed to verify this model.

References

Dziewonski, A. M. and D. L. Anderson (1981). Preliminary reference Earth model (PDF), *Physics of the Earth and Planetary Interiors*, 25(4) 297–356.

Hartzell, S. H., Heaton, T. H. (1983). Inversion of strong ground motion and teleseismic waveform data for the fault rupture history of the 1979 Imperial Valley, California earthquake. *Bulletin of the Seismological Society of America*, 73, 1553–1583.

IRIS DMC (2015). Data Services Products: Synthetics Engine, https://doi.org/10.17611/DP/SYNGINE.1.

Komatitsch, D., Tromp, J. (1999). Introduction to the spectral-element method for 3-D seismic wave propagation. *Geophysical Journal International*, 139, 806-822.

Lee, S. J., H. W. Chen, Q. Liu, D. Komatitsch, B. S. Huang, and J. Tromp (2008). Three dimensional simulations of seismic wave propagation in the Taipei basin with realistic topography based upon the spectral-element method, *Bull. Seismol. Soc. Am.* 98 253–264. http://dx.doi.org/10.1785/0120070033.

Lee, S. J., Ma, K. F., Chen, H. W. (2006). Three-dimensional dense strong motion waveform inversion for the rupture process of the 1999 Chi-Chi, Taiwan, earthquake. *J. Geophys. Res.: Solid Earth* (1978–2012) 111, B11.

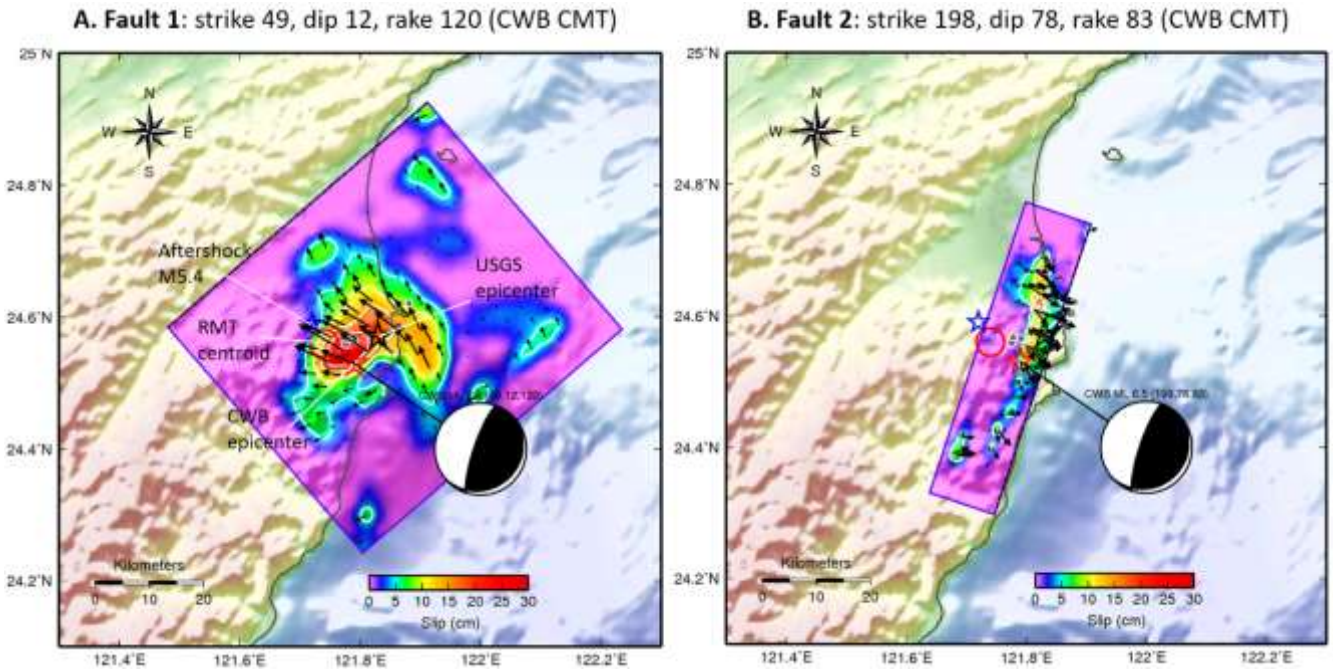

Figure 2.1 The slip distribution of the 2021 M_L6.5 Nanao earthquake. (A) Fault 1, and (B) Fault 2. The red star indicates the CWB epicenter of this event and the red open circle represents its centroid determined by RMT. The biggest aftershocks (M_L5.4) occurred one minute after the mainshock and later aftershocks are shown by a blue open star and gray circles, respectively. Blue open rectangles indicate the two fault planes (Fault 1, Fault 2) taken from CWB CMT. Their shallowest portions are shown by dotted lines.

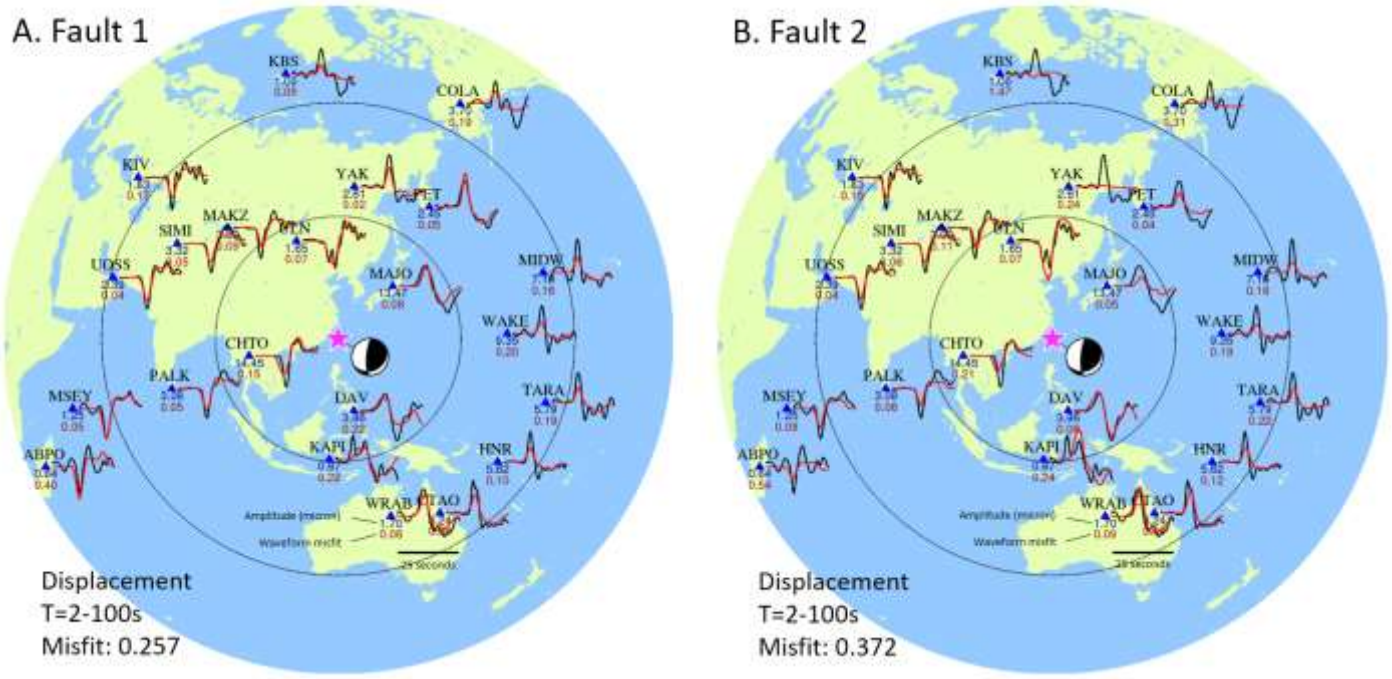

Figure 2.2 Comparison between the observed and synthetic teleseismic P wave displacement waveforms: (A) Fault 1, and (B) Fault 2. The black lines denote the observations, and the red lines represent the synthetics. The IRIS GSN waveforms are band-pass filtered between 0.01 and 0.5 Hz. A 25 seconds time window starts from 10 seconds before P and 15 seconds after P arrival was used in the inversion. The maximum amplitude of the observation (blue number) and waveform misfit (red number), defined as $(Ax\text{-}b)^2/b^2$, are shown at each station. The waveform misfit of Fault 1 and Fault 2 are 0.257 and 0.372, respectively.

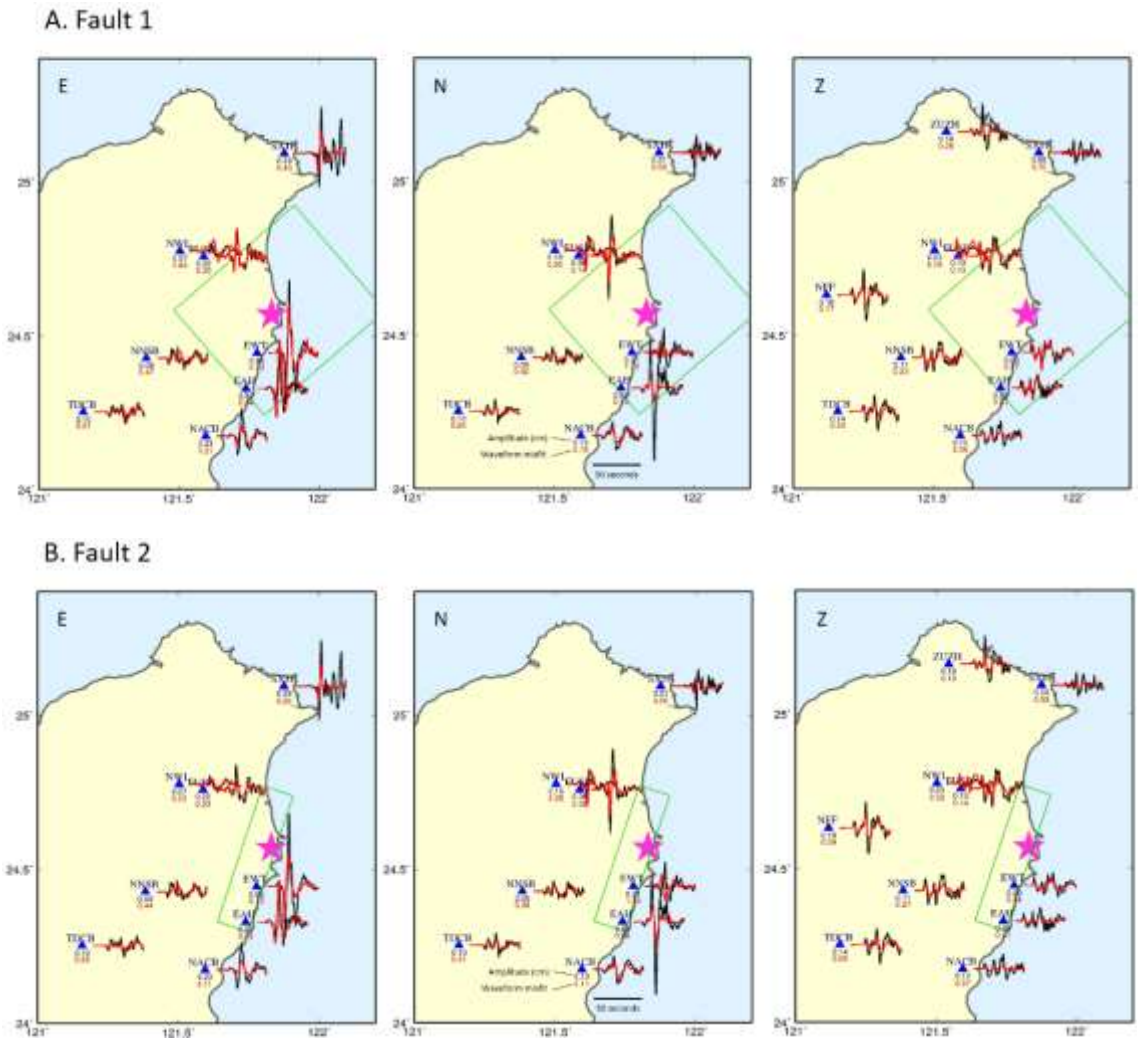

Figure 2.3 Comparison between local observation and synthetic waveforms in three components: (A) Fault 1, and (B) Fault 2. The black lines are BATS and CWB 24-bit observations, and the red lines are synthetic waveforms. All the waveforms are in the type of displacement and a band-pass filter with the period between 2 and 20 seconds was applied. The maximum amplitude of the observed displacement waveform and misfit between observation and synthetic are shown at each station. The pink star and green open rectangular are the epicenter and the fault plane projected to the surface, respectively. The waveform misfit of Fault 1 is 0.546, and Fault 2 is 0.498.

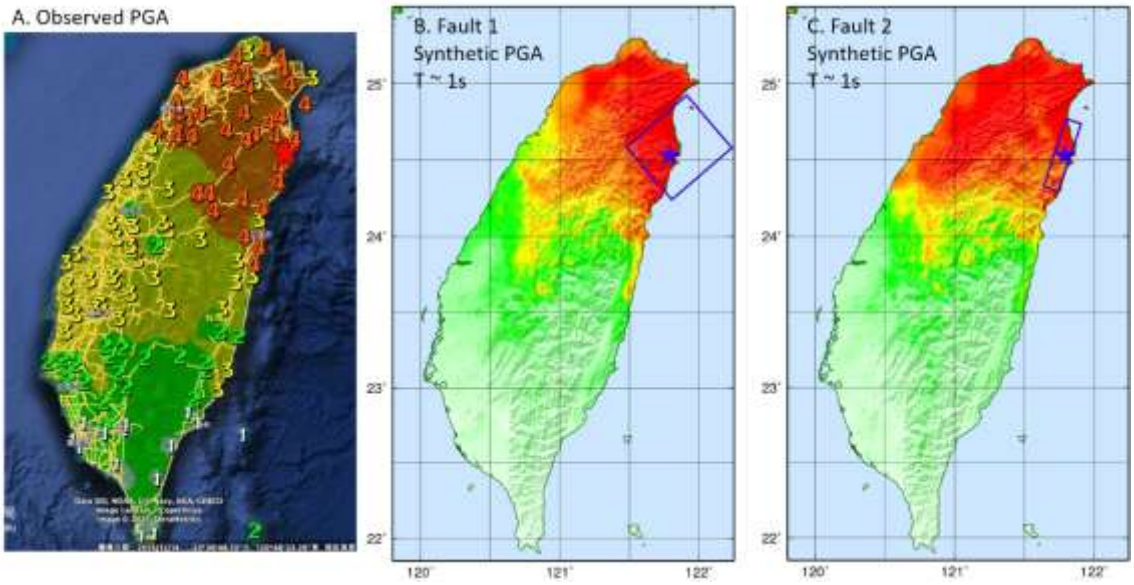

Figure 2.4 (A) Intensity map of the CWB earthquake report. (B) Synthetic PGA distribution derived from the finite-fault rupture model of Fault 1. (C) Synthetic PGA distribution derived from the finite-fault rupture model of Fault 2. The blue star and open rectangular are the epicenter and the fault plane projected to the surface, respectively.

Part 3.

The relationship between the Shoufeng earthquake swarm and the slip distribution of major earthquakes in eastern Taiwan in recent years

During the past ten years, there have been several major earthquakes that occurred in eastern Taiwan, including the October 31, 2013 Ruisui earthquake (M6.4), the May 21, 2014 Fenglin earthquake (M5.9), the February 6, 2018 Hualien offshore earthquake (M6.3), April 18, 2019 Hualien earthquake (M6.1), and the April 18, 2021 Shoufeng earthquake (M6.2) (Table 3.1). The distribution of these earthquakes extends from the northern Longitudinal Valley to Ruisui, showing that this is an area where large earthquakes frequently occur (Figure 3.1). Putting the possible fault planes of these earthquakes together, we can see that these fault planes almost cover the entire north to middle section of the Longitudinal Valley.

2013 Ruisui earthquake

Figure 3.2 shows the slip and aftershock distributions of the 2013 Ruisui earthquake. The largest asperity occurred in the northern area of the epicenter and most of the aftershocks occurred along the boundary of this asperity. Further to the north is the 2014 Fenglin earthquake, and the slip was relatively small in that area. Because the magnitude of 2014 Fenglin earthquake was only M5.9, it can be treated as a big aftershock after the 2013 Ruisui earthquake. Compare the aftershocks of the 2013 Ruisui earthquake with the 2021 Shoufeng earthquake, they are both located beneath the Central Range, but the aftershocks that occurred after 11 June 2021 were further to the north. It seems that there is no direct connection between these two aftershock groups.

2018 Hualien offshore earthquake

The slip and aftershock distributions of the 2018 Hualien offshore earthquake are complex which both show a northeast to southwest trend (Figure 3.3). Aftershock distribution almost filled the slip zone except for the asperity areas. Several deep aftershocks can be observed in the northern fault plane. The other group of aftershocks was found at the eastern offshore where no fault plane exists. These aftershocks might be caused by other seismogenic structures that were induced by the mainshock. The 2021 earthquake swarm happened to be located on the northern section of the Lingding Fault. This location also produced a considerable slip during the 2018 earthquake. Thus, it can be suspected that the 2021 earthquake swarm could also be related to the northern Lingding Fault.

2019 Hualien earthquake

The aftershock and slip distribution of the 2019 Hualien earthquake mainly occurred north of the epicenter (Figure 3.4). At the same time, the depths of both are relatively

deep (below 20 kilometers). If viewed from an east-west section, the aftershocks are obviously downward-dipping to the west, so it is inferred that this event was related to the Central Range Fault. But due to the slip and aftershocks are a bit distant from the 2021 earthquake swarm, the correlation between these two events is small.

2021 Shoufeng earthquake

The rupture of the 2021 Shoufeng earthquake started from the hypocenter and propagated bilaterally to the north and south (Figure 3.5). Most of the aftershocks occurred beneath the hypocenter and the southern part of the fault. There is almost no slip and aftershock occurred in the shallow fault plane. This implied the rupture didn't extend to the ground surface. However, after June 11, another group of aftershock (earthquake swarm) occurred in the northeast of the epicenter. This earthquake swarm happened to be in the shallow crust where there is no slip occurred during the April 11 mainshock. Does this mean that this swarm is related to the west-dipping fault plane where the mainshock ruptured or there is aother east-dipping fault (the Lingding Fault)? This problem requires more follow-up aftershocks and geological data to joint interpretation.

Discussion

It is worth noting that after the 2018 Hualien offshore earthquake, the Coulomb stress is increased in the Longitudinal Valley, regardless of the fault plane that dips eastward or westward (Figure 3.6). In other words, after the 2018 event, the probability of subsequent earthquakes in this area is increased. Returning to the relationship between the slip distribution of major earthquakes and the 2021 earthquake swarm, there are still some seismic gaps in eastern Taiwan (the question marks in Figure 3.7), i.e. no slip or aftershocks have occurred in those areas. In addition, the recent big events all occurred in the northern section of the Longitudinal Valley, and the southern section is relatively quiet. So, has the seismic potential of the central to the southern section of the Longitudinal Valley increased? Will there be bigger earthquakes in the future? All these issues must continue to be paid high attention.

References

Lee, S. J., T. P. Wong, T. Y. Liu, T. C. Lin and C. T. Chen (2019, Oct). Strong ground motion over a large area in northern Taiwan caused by the northward rupture directivity of the 2019 Hualien earthquake. Journal of Asian Earth Sciences.

Lee, S. J., T. C. Lin, T. Y. Liu and T. P. Wong (2018, Sep). Fault-to-Fault Jumping Rupture of the 2018 Mw 6.4 Hualien Earthquake in Eastern Taiwan. Seismological Research Letters , 90(1), 30-39.

Lee, S. J. (2017, Oct). Lessons Learned from Source Rupture to Strong Ground Motion Simulations: An Example from Taiwan. Bulletin of the Seismological Society of America, 107, 2106-2116.

Lee, S. J., H. H. Huang, J. Bruce H. Shyu, T. C. Lin, and T. Y. Yeh (2014, Dec). Numerical earthquake model of the 31 October 2013 Ruisui, Taiwan, Earthquake: Source rupture process and seismic wave propagation. Journal of Asian Earth Sciences, 96, 374-385.

Table 3.1 The source parameters of major earthquakes in eastern Taiwan in recent years

時間	經度	緯度	深度	規模 ML	走向	滑移	傾角
2013/10/31	121.35	23.57	15.0	6.4	209.15	59.41	51.35
2014/05/21	121.43	23.74	16.5	5.9	208.05	60.23	58.47
2018/02/06	121.730	24.10	6.31	6.26	215.68	56.36	25.57
2019/04/18	121.54	24.06	18.8	6.1	204.0	63.0	66.0
2021/04/18	121.48	23.86	13.9	6.2	199.9	52.6	53.7

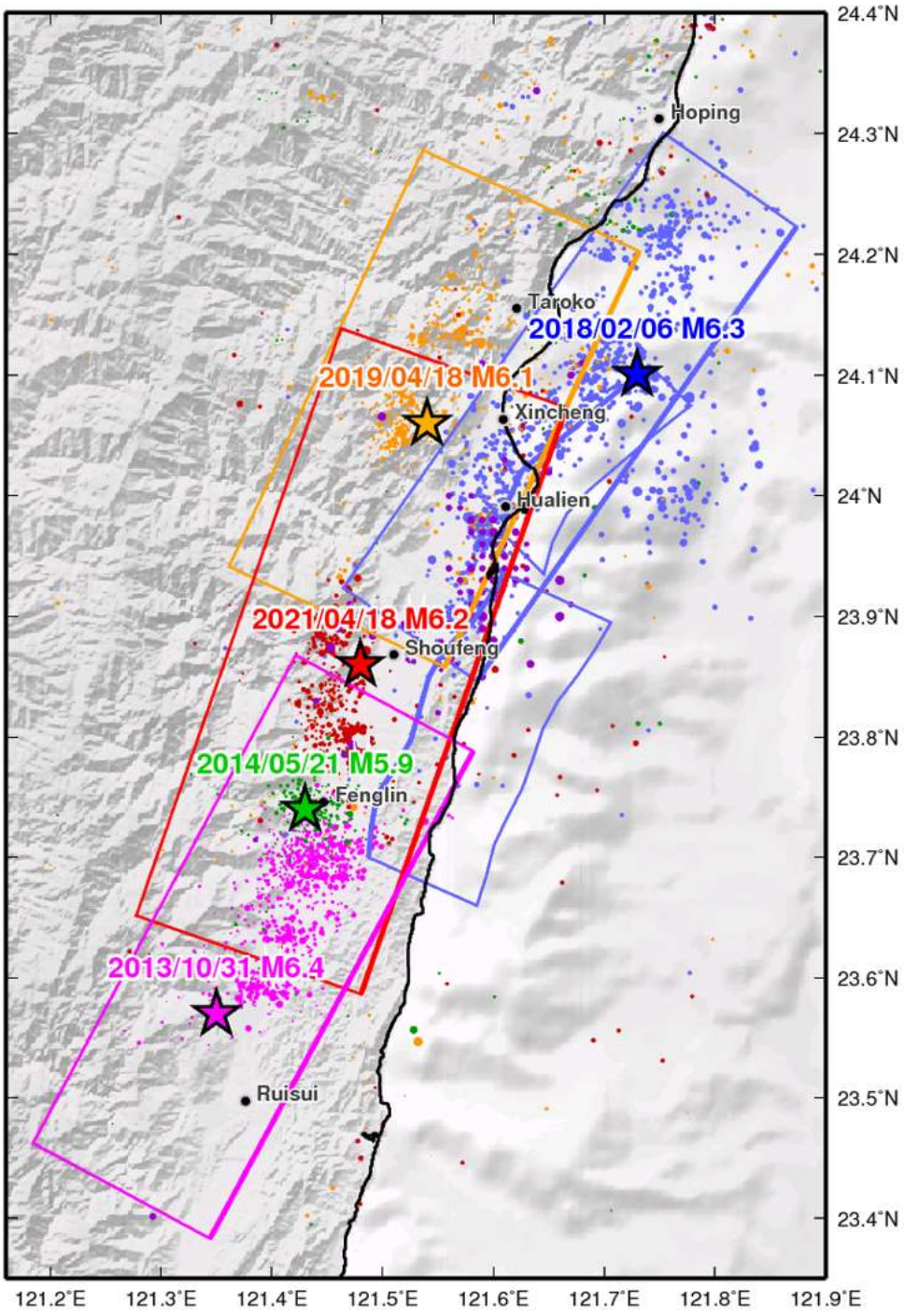

Figure 3.1 The epicenters, aftershocks, and fault planes of the major earthquakes in eastern Taiwan in recent years. The colored stars and circles are the epicenter and the aftershock of each event, respectively.

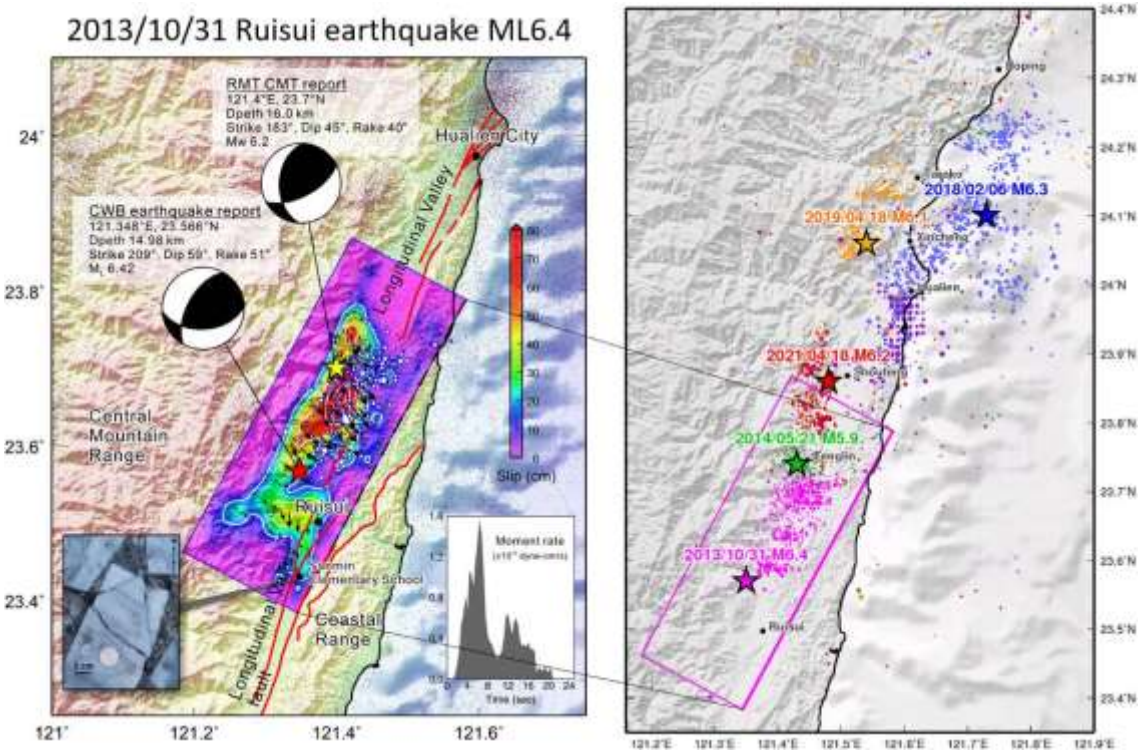

Figure 3.2 The slip and aftershock distributions of the October 31, 2013 Ruisui earthquake M6.4. The red star shows the CWB epicenter and the yellow star indicates the RMT centroid.

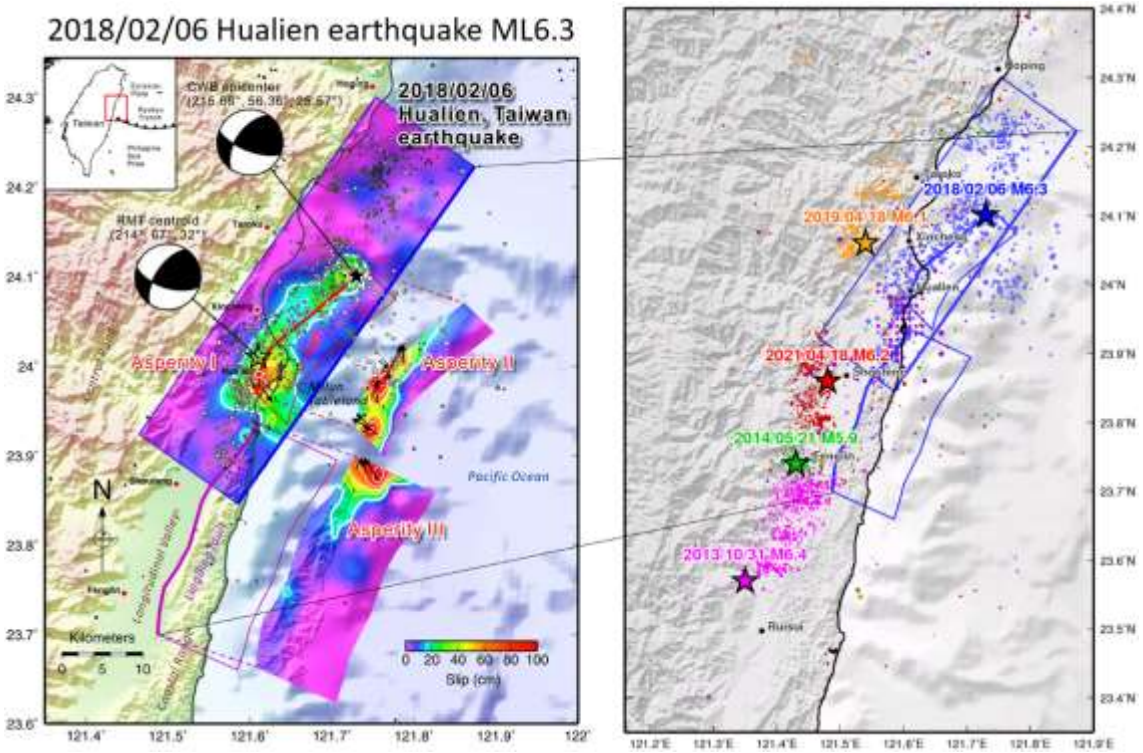

Figure 3.3 The slip and aftershock distributions of the February 6, 2018 Hualien offshore earthquake M6.3. The black solid star shows the CWB epicenter and the open star indicates the RMT centroid.

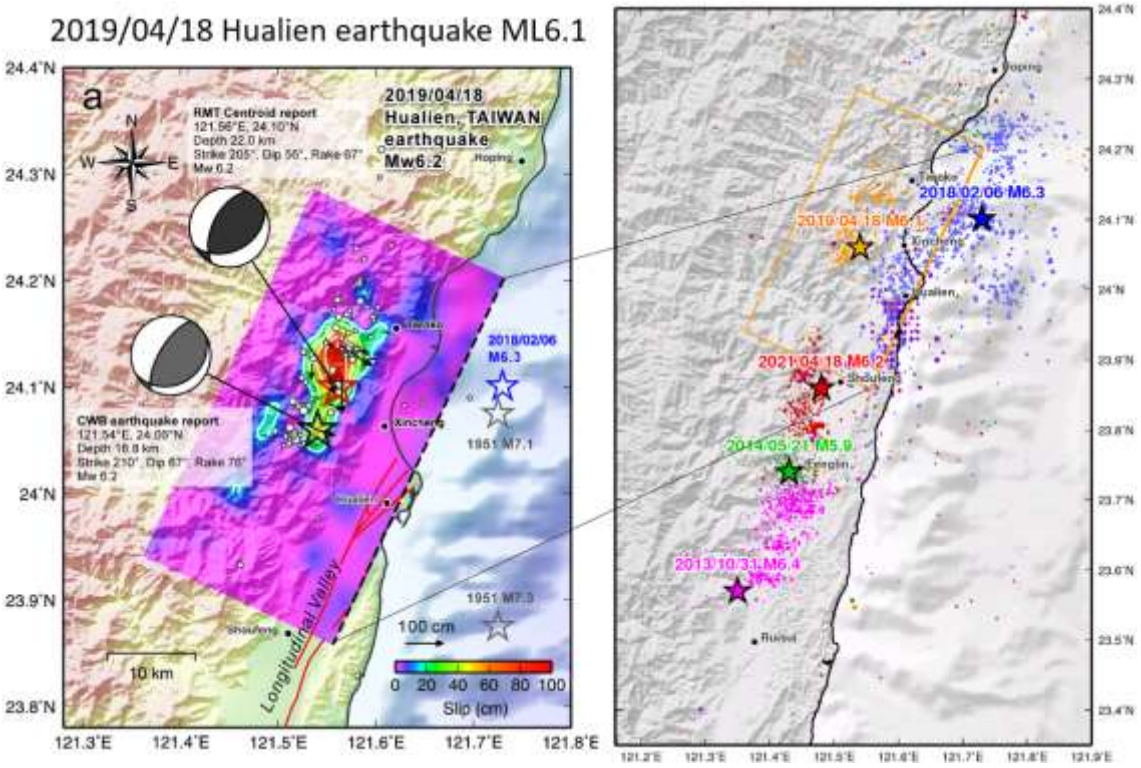

Figure 3.4 The slip and aftershock distributions of the April 18, 2019 Hualien earthquake M6.1. The black open star shows the CWB epicenter and the red open star indicates the RMT centroid.

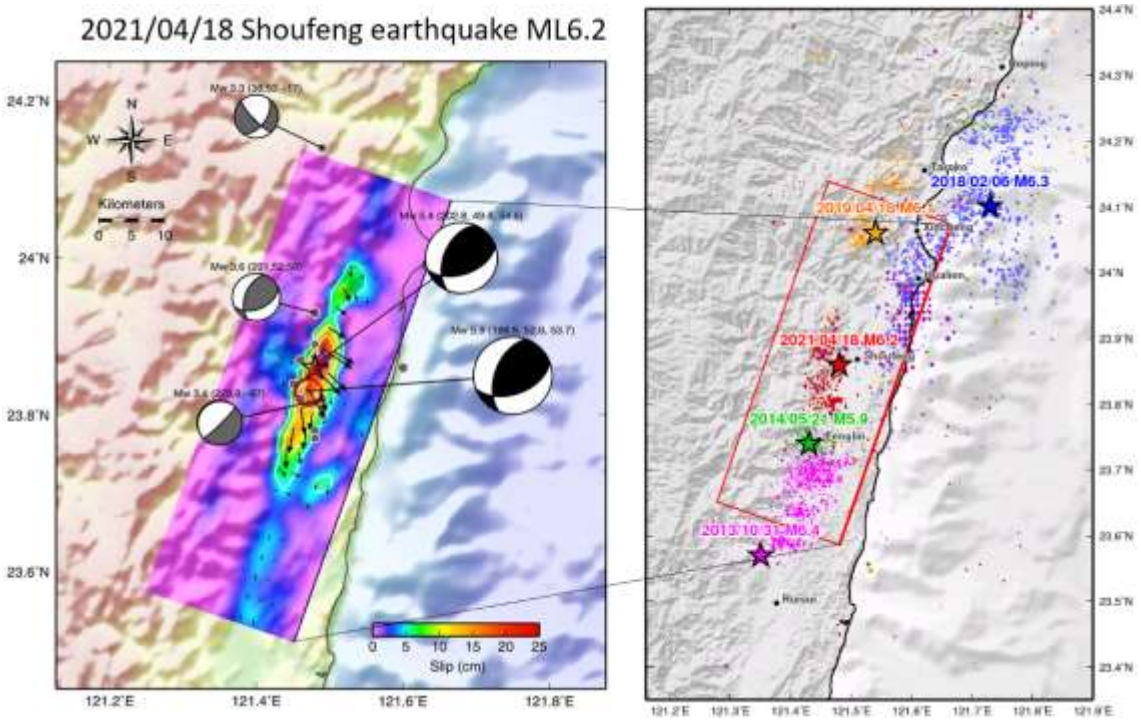

Figure 3.5 The slip and aftershock distributions of the April 18, 2021 Shoufeng earthquake M6.2. The black open star shows the CWB epicenter and the red open circle indicates the RMT centroid.

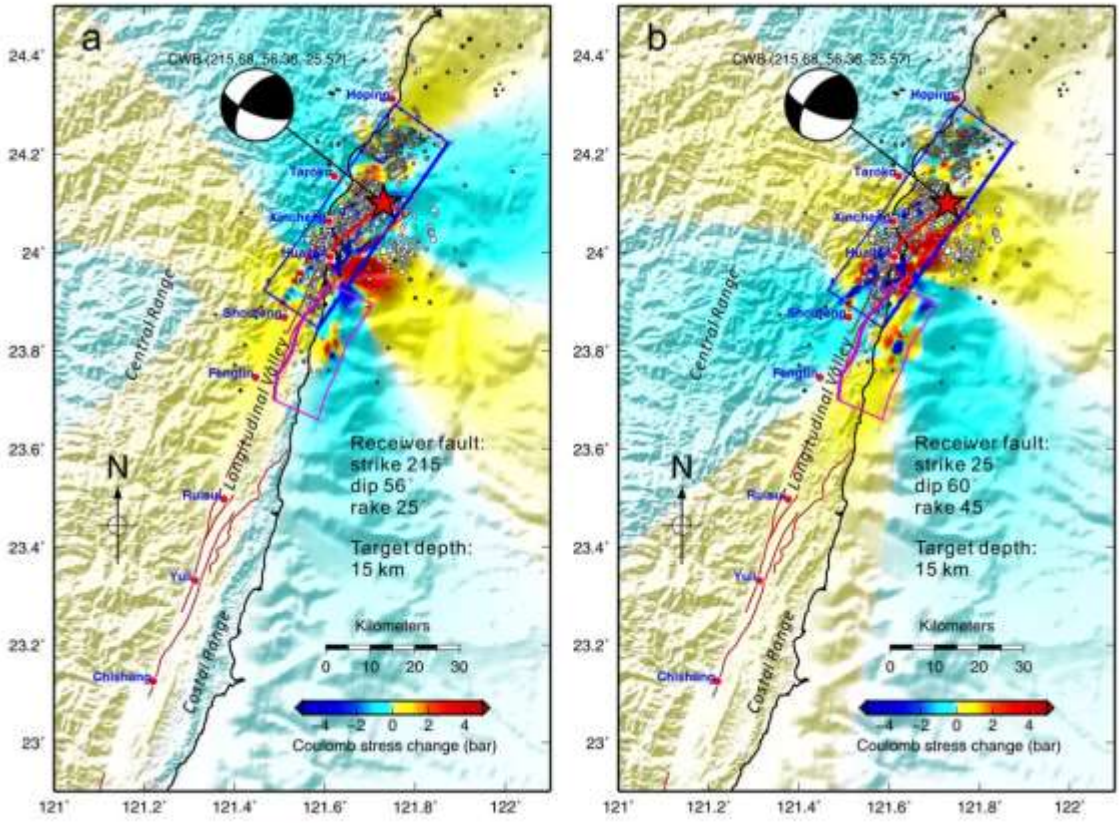

Figure 3.6 The result of Coulomb stress changes caused by the 2018 Hualien offshore earthquake. The CWB epicenter is indicated with a red star. Two different receiver fault plane mechanisms at depths 15 km were considered: (a) the N-S striking, east-dipping fault (strike 215°, dip 56°, rake 25°) that is close to the geometry of the Central Range Fault, (b) the Lingding Fault (strike 25°, dip 60°, rake 45°), which is close to the mechanism of the east-dipping Longitudinal Valley Fault.

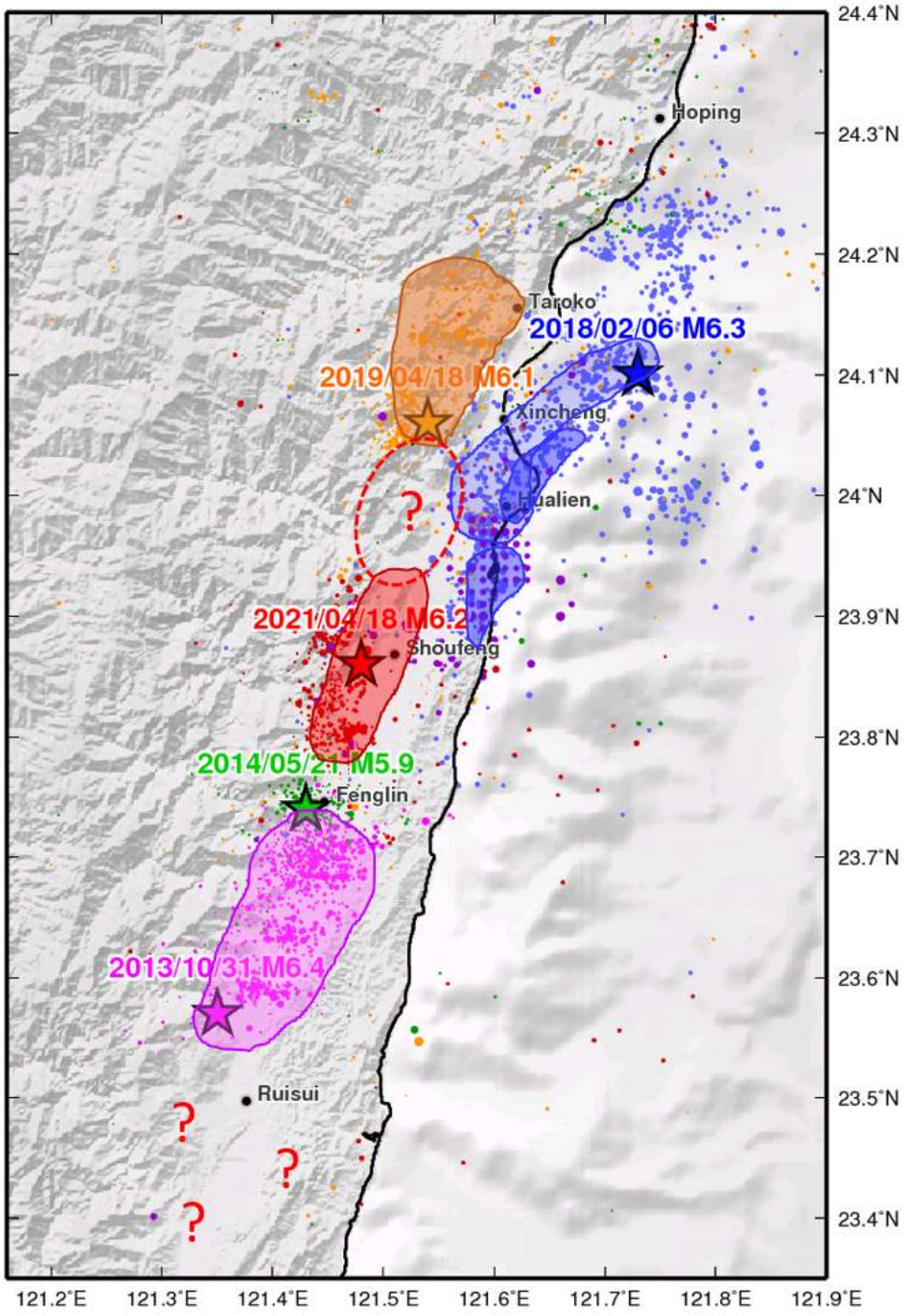

Figure 3.7 The epicenters, aftershocks, and rupture areas of the major earthquakes in eastern Taiwan in recent years. The colored stars, circles, and translucent areas are the epicenter, aftershock, and rupture area of each event, respectively. The red question marks indicated the location of seismic gap.

臺灣地區 110 年中大型地震震源資訊之快速彙整與提供

子計畫二

運用深度學習方法開發現地型地震預警系統

金台齡 吳祖霆 江又靖 郭明樹

臺灣科技大學

1 中文摘要

臺灣地震發生的頻率非常高，破壞性的地震往往會帶來重大的損失，而能有效減少這些地震災害的方法為地震預警系統，能夠在這些強震波發生之前提供警告，來減少地震災害。地震預警系統又可以分成兩種類型，一種是區域型預警，另一種則為現地型預警，區域型預警系統會收集震央附近測站的資訊，如果偵測到強烈震波，系統可對較遠的地方發送警報，但面臨到的問題是，近震央的區域無法及時收到警報，會形成一個預警盲區，等到警報發出的時候，地震可能已經結束。為了解決預警盲區的問題，因此需要現地型預警系統，能夠為近震央區域提供預警，希望每一個地震測站收到地震波的很短的時間內，就可以預測出將來會不會發生劇烈地搖晃，實際上會使用初始 P 波信號來預測最大的地面運動，傳統方法是學者使用直覺或經驗選擇的某些標準來進行預測。但是，這些標準很難選擇，而且預測的準確性也很容易會受到這些標準的影響。本文研究了基於神經網路的方法，在 P 波到達地震測站後及早預估地震動的最大地面運動。建立模型以使用初始 P 波加速度信號的幾秒鐘時間窗口進行預測，該模型由臺灣 1991 年至 2019 年採集的地震波進行訓練，並透過 2020 年和 2021 年的事件進行評估。從評估結果來看，所提出的方案在準確性和平均預警時間方面皆明顯優於傳統基於閾值的方法。此外，本文也嘗試將此模型部屬至 earthworm 地震預警系統，並結合 LINE 通知，在一個測站偵測到強震波的到來時，便會即時傳送通知，告知預測結果，達到現地型預警的目的。

2 英文摘要

Onsite earthquake early warning is a challenging problem since the limited time and information collected before the warning determination. A potential solution to prevent severe disasters is to predict the greatest ground motion using the initial P--wave signal and provide warnings before the hit of the shaking. In practice, the

accuracy of the prediction is the most critical issue for earthquake early warning systems. Traditional methods use certain criteria selected by intuition or experience to make the prediction. However, the thresholds for the criteria are difficult to select and may significantly affect the accuracy. This study investigates the methods based on artificial intelligence to predict the greatest ground motion of earthquakes at the early stage when the P-wave arrives at the seismograph stations. A neural network model is built to make the predictions using a small window of the initial P-wave acceleration signal. The model is trained by the seismic waves collected from 1991 to 2019 in Taiwan and evaluated by events in 2020 and 2021. From the evaluations, the proposed scheme significantly outperforms the threshold-based method in terms of the accuracy and the average leading time. In addition, this study integrates the proposed scheme with Earthworm monitoring system. The predictions are sent by LINE notifications to emulate onsite earthquake early warnings.

3 前言

嚴重的地震常常造成財務與生命的重大損失，在強震波到來前發布警報是可以降低損失的一種可能的方式，區域型預警系統通常會在震央附近偵測到地震時發布警報至遠處。然而，靠近震央的預警盲區便會有可能遭受巨大的損失，因此，現地型預警的方法是一個重要的研究課題。

在過去十年，部分學者已找出地震規模與初始 P 波訊號的關聯，一些研究已指出透過前數秒的 P 波訊號計算出的地震規模與地震事件的實際規模呈正比關係，如使用 Peak Ground Displacement (Pd) 方法在給定初始 P 波訊號下計算規模，可作為估計地震規模的一個基準，或使用 Pd 方法作為閥值並結合時間參數 τ_c 以進行地震波預警，兩個方法皆快速提供警告，期望在地震波到達劇烈晃動前提供充足的反應時間，然而，這些參數的標準很難選擇，而且預測的準確性也很容易會受到這些標準的影響導致誤判或遺漏，這些標準通常由專業人員根據經驗或直覺所挑選出來，可能無法涵蓋所有的地震資訊。因此，我們研究一個基於人工智慧的方法，以從初始 P 波訊號中獲得更多的資訊。

在本研究中，我們提出 Intelligent ground motion prediction (IGMP) 方法來預估地震動，本方法試圖利用 Convolutional Neural Network (CNN) 技術找出強震波與 P 波間的關係，輸入值為一組三軸的加速度資料，與傳統方法相比，本方法可以從多個不同軸的資料同時截取更多有用的特徵值，儘管這些特徵值可能無顯著物理意義，卻可以讓模型據以分辨出強震波。本 IGMP 方法利用前幾秒的 P 波時間窗來預測接下來地震波的最大 Peak Ground Acceleration (PGA) 是否會超過一定的閥值。該模型利用 1991 年至 2019 年的臺灣強地動觀測網 (TSMIP) 以及 2014 年至 2019 年的 CWB 觀測網 (CWBSN) 資料進行訓練及測試，此外亦使用 2020 年至 2021 年的 CWBSN 之資料，作為本模型的效能評估資料。

本研究方法根據不同長度的時間窗格進行了效能的評估，從結果來看，本方法不管在準確度或是平均的 Leading time 皆優於傳統方法，在測試資料中，本方法較傳統方法產生更多正確的預警報告，也有著更多的 leading time，這表

示本方法可從地震波中截取更多關鍵資訊以預測潛在的強震。

4 類神經網路應用於現地型地震預警

4.1 簡介

本研究目的是希望利用 P 波初達後數秒內的資料,結合類神經網路的技術,來預測震央附近測站的 PGA 是否達到 80 Gal 以上，如果近震央處幾公里內有幾個測站皆有達標，即可立即對近震央區域發警報，並對其他較遠區域提供更快速的預警，來增加反應時間。

4.2 資料處理

本研究使用的資料集來自兩個觀測網，第一個為中央氣象局 CWB 觀測網中，時間從 2014/01/01 到 2019/12/31 的測站紀錄，包含加速度地震儀、寬頻速度地震儀、短周期速度地震儀，其測站分布如圖 1 所示，總共有 896 筆事件；而第二個為臺灣強地動觀測網(TSMIP)中，時間從 1991 年至 2019 年的測站紀錄，其測站分布如圖 2 所示，總共有 724 筆事件。

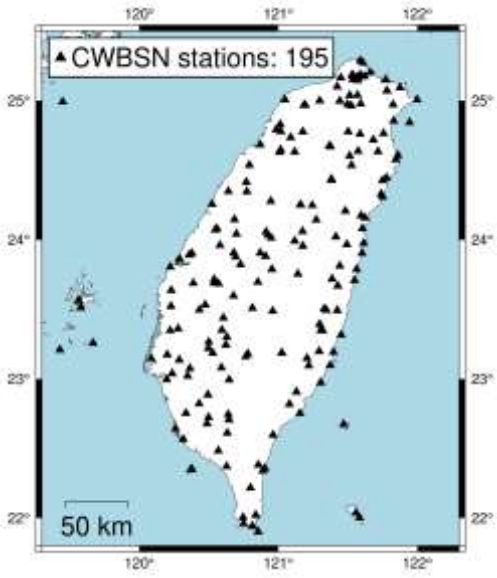

圖 1 CWB 測站分布

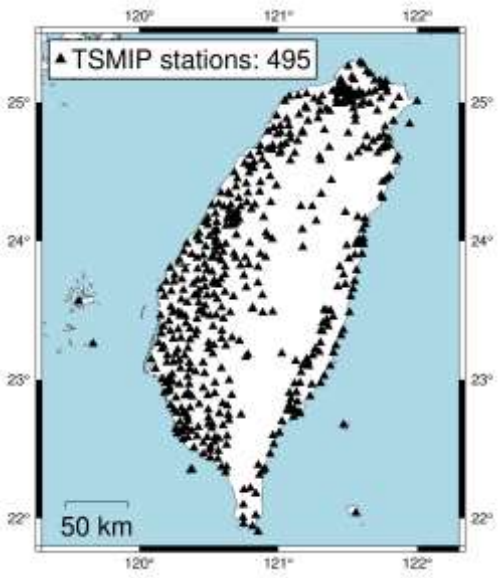

圖 2 TSMIP 測站分布

在本次研究中,我們只使用規模大於(包含)4 且震源深度範圍在 0~270km 的紀錄，其規模和深度分布如圖 3 圖 4 所示。

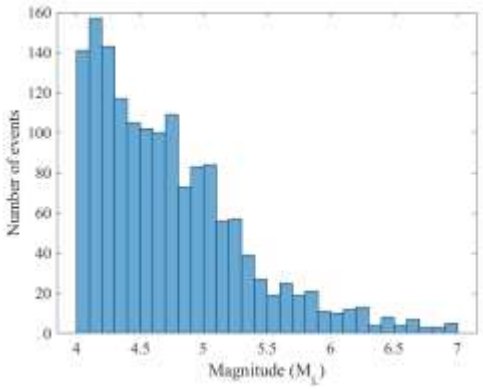

圖 3 規模分布圖

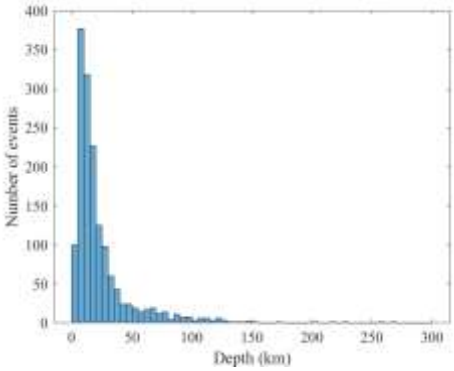

圖 4 深度分布圖

而事件的位置分布如圖 5 所示，其中規模大小會由圓圈大小表示、深度會由顏色深淺表示。

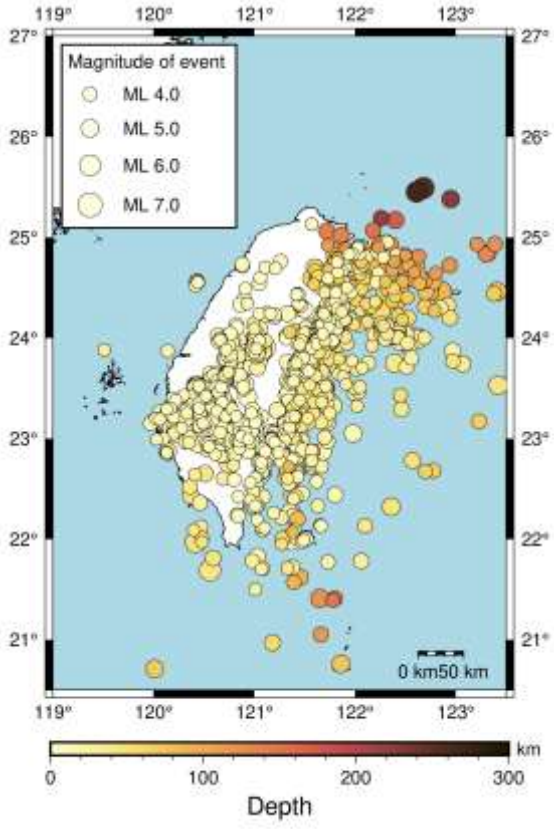

圖 5 事件位置分布圖

對於資料集中的資料，我們必須事先做資料處理。首先，我們會將收集到的原始波形資料減去平均值並乘上相對應的測站係數，針對速度資料，會將其微分成加速度資料，包含 CWB 觀測網中的寬頻速度地震儀和短周期速度地震儀，

然後將所有速度資料都過 0.075Hz 高通濾波，最後用三軸合成向量的最大振幅計算 PGA。每筆加速度資料都用 100Hz 進行採樣。為了平衡記錄的數量，我們將 $PGA < 80$ Gal 的資料標記成$[0, 1]$，$PGA \geq 80$ Gal 的資料標記成$[1, 0]$，來當作是資料的 Label。

最後總共有 8620 筆紀錄。為了提供給模型作訓練與測試，我們將資料分為訓練集和測試集，它們個別有 6900 和 1720 筆加速度紀錄，其 PGA 分布個別如圖 6 圖 7 所示。

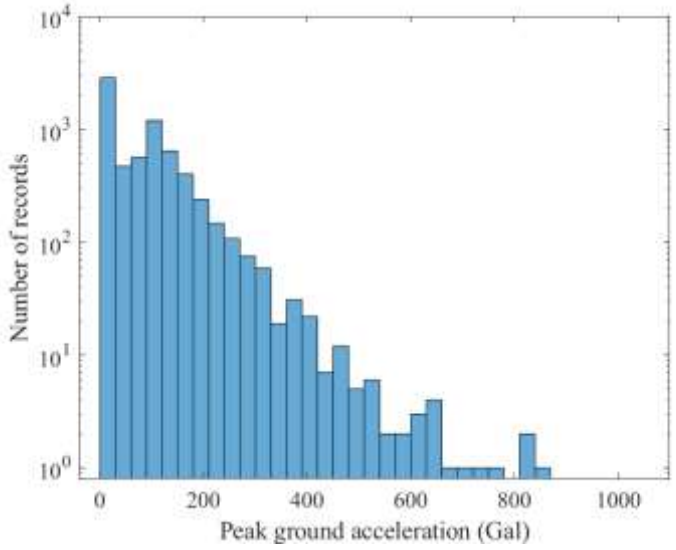

圖 6 訓練集 PGA 分布

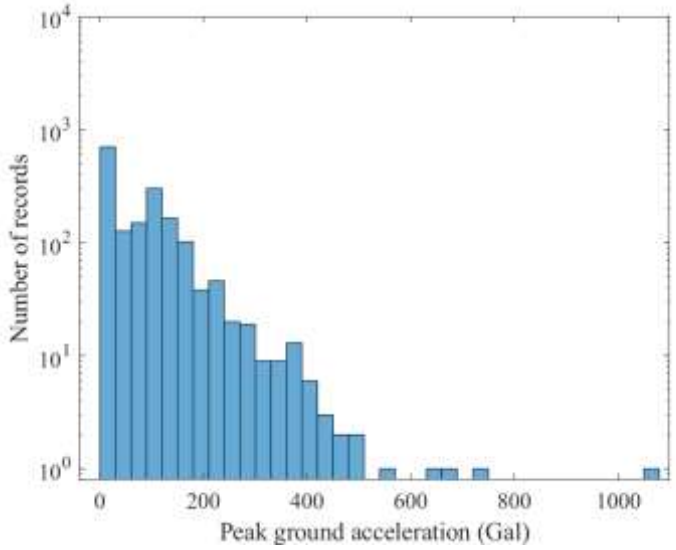

圖 7 測試集 PGA 分布

4.3 模型架構

本研究的模型架構圖如圖 8 所示，總共由輸入、特徵擷取器、分類、輸出四個部分組成。首先，模型會輸入由觀測網收集到的 P 波到時後 N 秒的三軸加速度資料，接者這些資料會經過兩層卷積神經網路，用來當作是地震訊號的特徵提取器。每層卷積神經網路中都包含三個單元，第一個是 kernel size 為 3、stride 為 2、channel 數量為 32 的一維卷積，第二個是 Batch Normalization，將每次迭代的每個 mini-batch 進行歸一化，目的就是還原出上一層需要學習的數據分布，最後使用整流線性單位函數（Rectified Linear Unit, ReLU）做為激勵函數。接著再進入到下一層卷積神經網路，與第一層的差別只是於一維卷積的 channel 數量改為 64。透過這些卷積層之後，模型便能根據波形學 P 波特徵，有了這些特徵後，接著用 Flatten 將學到的所有特徵攤平成一維陣列，然後輸入到全連接層中來彙整所有的特徵資訊，再接另一個全連接層將資料進行分類，最後輸出 2 分類的機率值，一個為 PGA < 80 Gal 的機率，另一個則為 PGA ≥ 80 的機率。

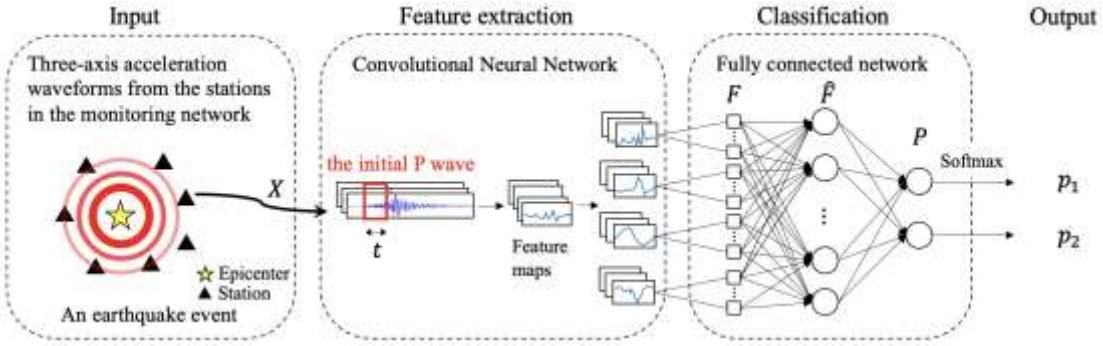

圖 8 模型架構圖

在訓練模型的過程中，使用的是 AdamW 優化器，損失函數為 Binary Cross Entropy loss，batch size 設為 100，而學習率初始值為 0.001，在每一輪訓練中學習率會慢慢下降，經 100 輪訓練後結束訓練。對於 P 波到達後 1、2、3、4、5 秒的資料，各自都會有其相對應的訓練模型。

4.4 具體成果

4.5.1 模型表現

在此實驗中採用 Precision、Recall、F1-score 等指標來進行評估，如果 Precision 的數值高則代表預測為正樣本中有很高的機率是真的正樣本；如果 Recall 高則代表能找出所有正樣本的機率高；F1-score 則是同時考慮了 Precision 和 Recall 的指標。

為了凸顯本研究模型(IGMP)的表現，另外使用了其他研究的方法來做比較，在此用來做比較的是傳統的 threshold-based 方法，名稱為 Pd 方法。比較結果如圖 9 所示，可以觀察到隨輸入資料的秒數提升，IGMP 的 F1-score 的比率也相對提升，在 3 秒時已經超越 85%，5 秒時甚至高達 90%。相比之下，不管在任何輸入秒數的情況下，Pd 用不同的 threshold 都沒辦法超越 IGMP。

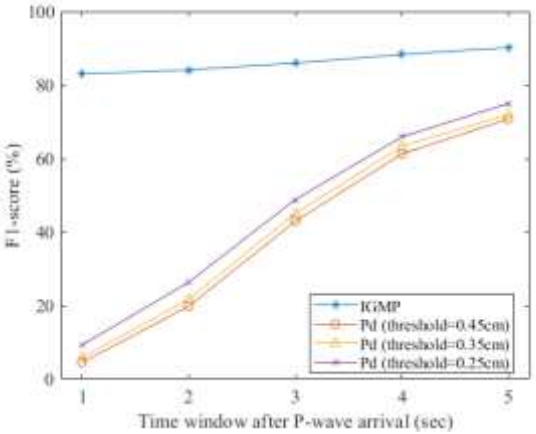

圖 9 各個方法的 F1-score 成果

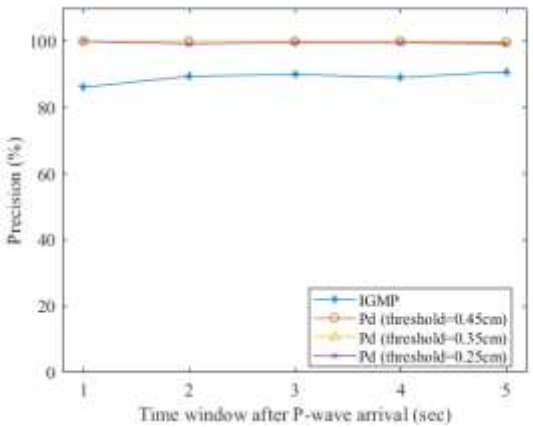

圖 10 各個方法的 Precision 成果

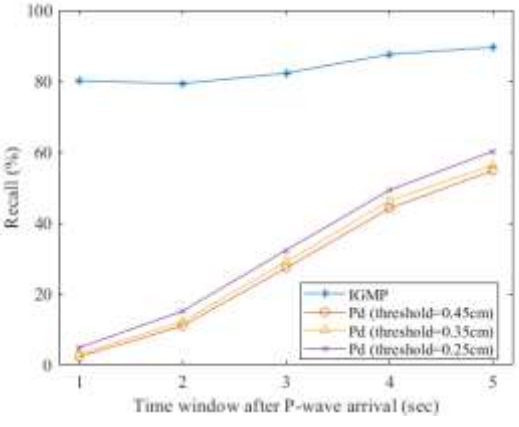

圖 11 各個方法的 Recall 成果

在 Precision 方面，其比較結果如圖 10，可以觀察到 IGMP 和 Pd 都有超過 85%的表現，代表它們發生錯誤警報的機率都較低。在 Recall 方面，其比較結果如圖 11，可以觀察到 IGMP 在任何輸入秒數的情況下 Recall 都超過 80%，表現比任何 threshold 的 Pd 都好。代表 IGMP 更有能力去判斷是否將要發生的地震，因此比 Pd 方法更適合用於地震預警系統。

4.5.2 模型的平均 Leading Time 表現

Leading Time 指的是輸入資料的結束時間到 PGA 最大震幅的時間，如果此時間越長，就代表抵達最大 PGA 前的時間就越長，能有更多的時間去反應、發警報等。在所有正確預測到的紀錄中，IGMP 與 Pd 的平均 Leading Time 比較如圖 12，可以觀察到 IGMP 在 1~4 秒的時候，Leading Time 比任何不同 threshold 的 Pd 都長，代表 IGMP 預測正確的樣本中，Leading Time 都較長。但在 5 秒的時候，Pd 比 IGMP 更長，這是因為 Pd 在這個情況下沒有正確預測到更多的紀錄，就如其 4 秒時一樣。

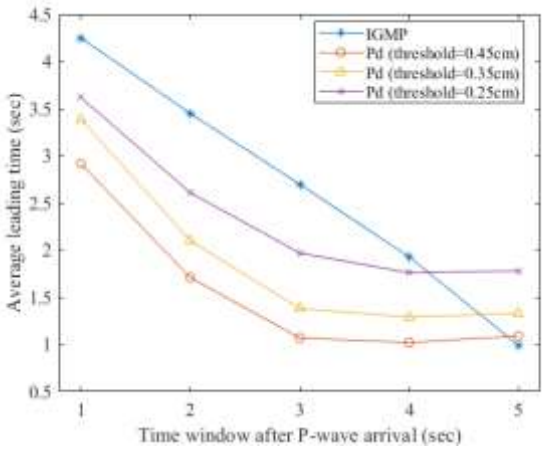

圖 12 各個方法的 Leading Time 成果

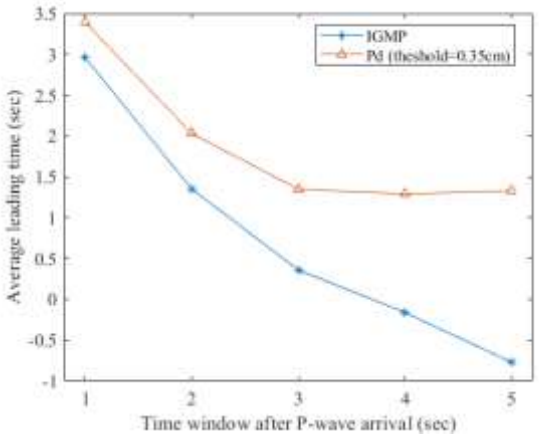

圖 13 兩方法皆有正確預測之事件 Leading Time 成果

如圖 13，在兩方法皆有正確預測的事件的情況下，雖然 threshold=0.35 公分的 Pd 在 Leading Time 上的表現比 IGMP 好，但 Pd 的 miss rate 較高，錯失很多 PGA 大於 80GAL 的事件。

4.5.3 花蓮地震事件預警測試

在此實驗中，我們使用 threshold=0.35 公分的 Pd 方法來與本論文方法(IGMP)做比較。我們使用 P 波到達後不同輸入時間長度的資料來進行測試，並應用於兩個不同地區的事件，評估其各自的表現。第一個我們選取 2021 年 4 月 18 日，規模 6.2，深度 11.4 公里的花蓮地震做預警測試，如圖 14 所示，藍色三角形代表 PGA<80 的紀錄，在此次事件中共有 134 個、紅色方塊代表 PGA≥80 的紀錄，在本次事件中共有 12 個。

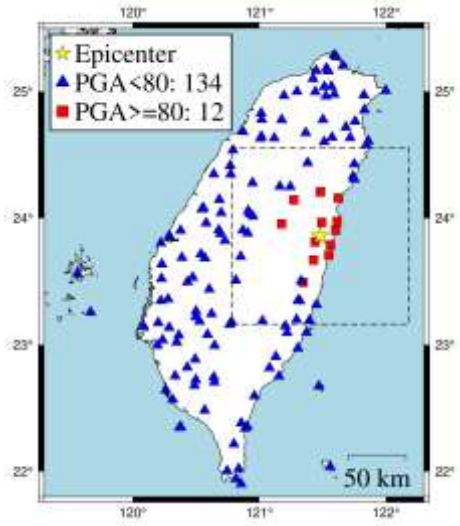

圖 14 花蓮地震的 PGA 數值和分布圖

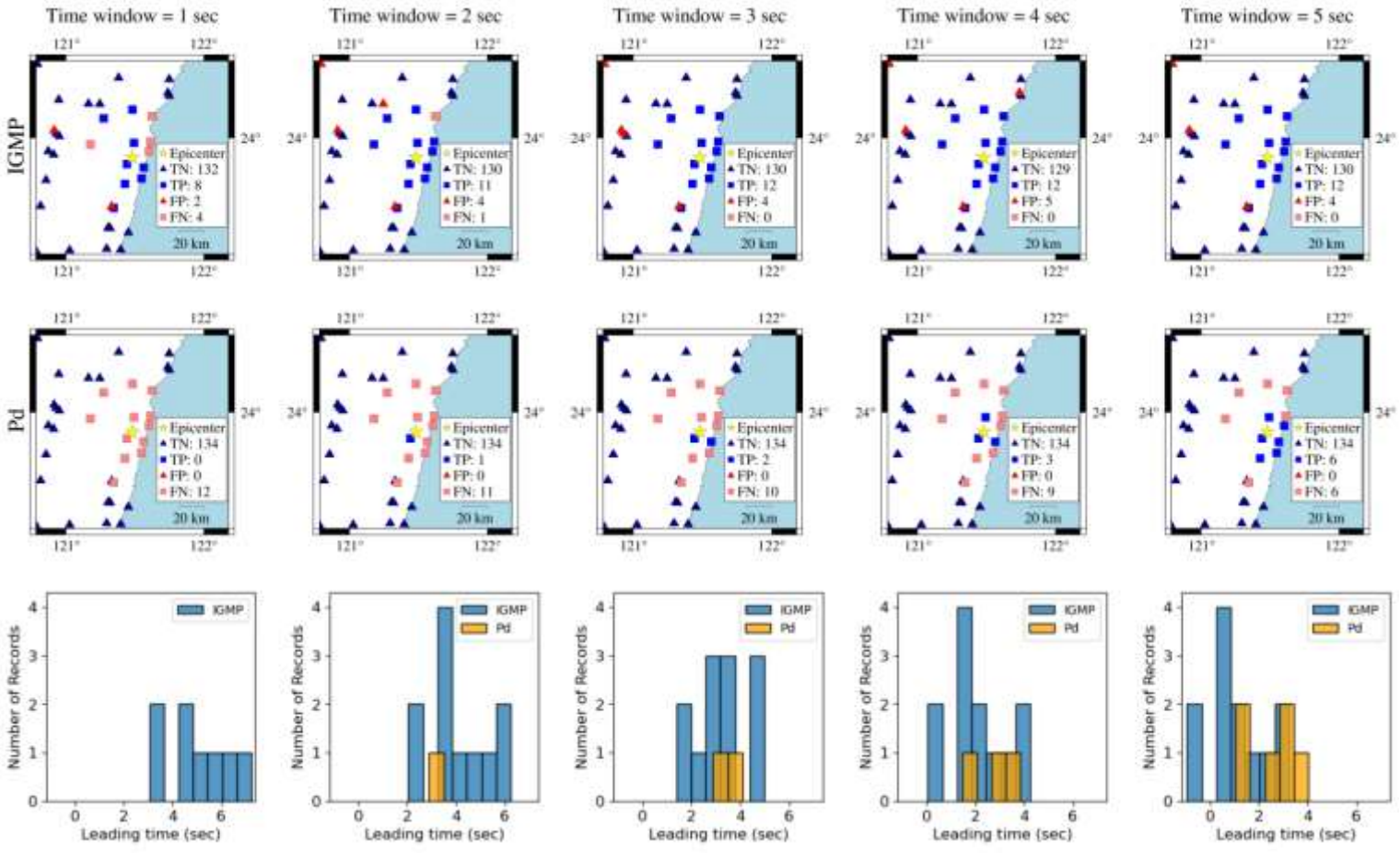

圖 15 花蓮地震的模型預測結果及其 Leading Time

放大震央附近的區域來看，如圖 15 所示，可以觀察到 IGMP 在輸入時間

長度為 1 秒時，可以成功的預測出震央附近 8 個測站的 PGA≥80，長度為 3 秒以上時，甚至可以預測出所有 PGA≥80 的測站。相比之下，Pd 在 1 秒時沒辦法正確預測出所有測站，因此也沒有 Leading Time，長度為 3 秒時也只能預測出 2 個測站。

如圖 15 的第三列，隨者輸入時間變長，Leading Time 也會相對變短。以 IGMP 為例，輸入時間長度為 1、2、3、4、5 秒時，個別有 4.97、4.1、3.12、2.12、1.12 的平均 Leading Time，因此要視情況選擇合適的輸入時間。

4.5.4 臺東地震事件預警測試

在此實驗中，我們使用 threshold=0.35 公分的 Pd 方法來與本論文方法(IGMP)做比較。我們使用 P 波到達後不同輸入時間長度的資料來進行測試，並應用於兩個不同地區的事件，評估其各自的表現。第二個我們選取 2021 年 1 月 17 日，規模 5.5，深度 21.1 公里的臺東海外地震做預警測試，如圖 16 所示，藍色三角形代表 PGA<80 的紀錄，在此次事件中共有 99 個、紅色方塊代表 PGA≥80 的紀錄，在本次事件中共有 0 個。

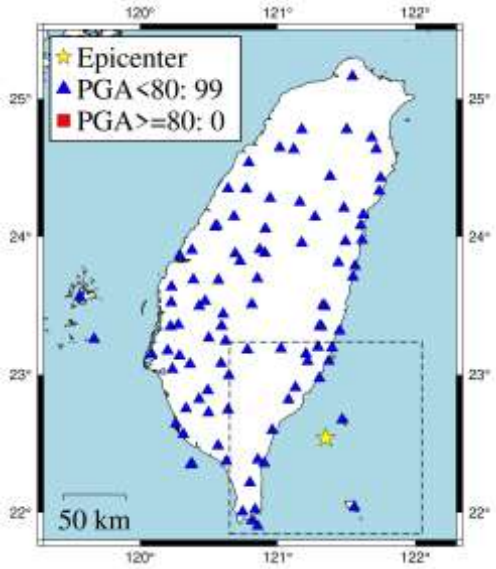

圖 16 臺東海外地震的 PGA 數值和分布圖

放大震央附近的區域來看，如圖 17 所示，可以觀察到 IGMP 在輸入時間長度為 1~3 時錯誤警報逐漸下降，3~5 秒時沒有變化，代表 IGMP 在 3 秒就已經有足夠的資訊去做判斷。唯一一個持續錯誤警報的測站是因為其 PGA 很接近 80 Gal，代表 IGMP 有能力可以發現潛在的地震危險，而 Pd 雖然能在所有輸入時間長度的情況下，正確預測出所有紀錄，卻沒辦法像 IGMP 一樣能判別出潛在的地震危險。

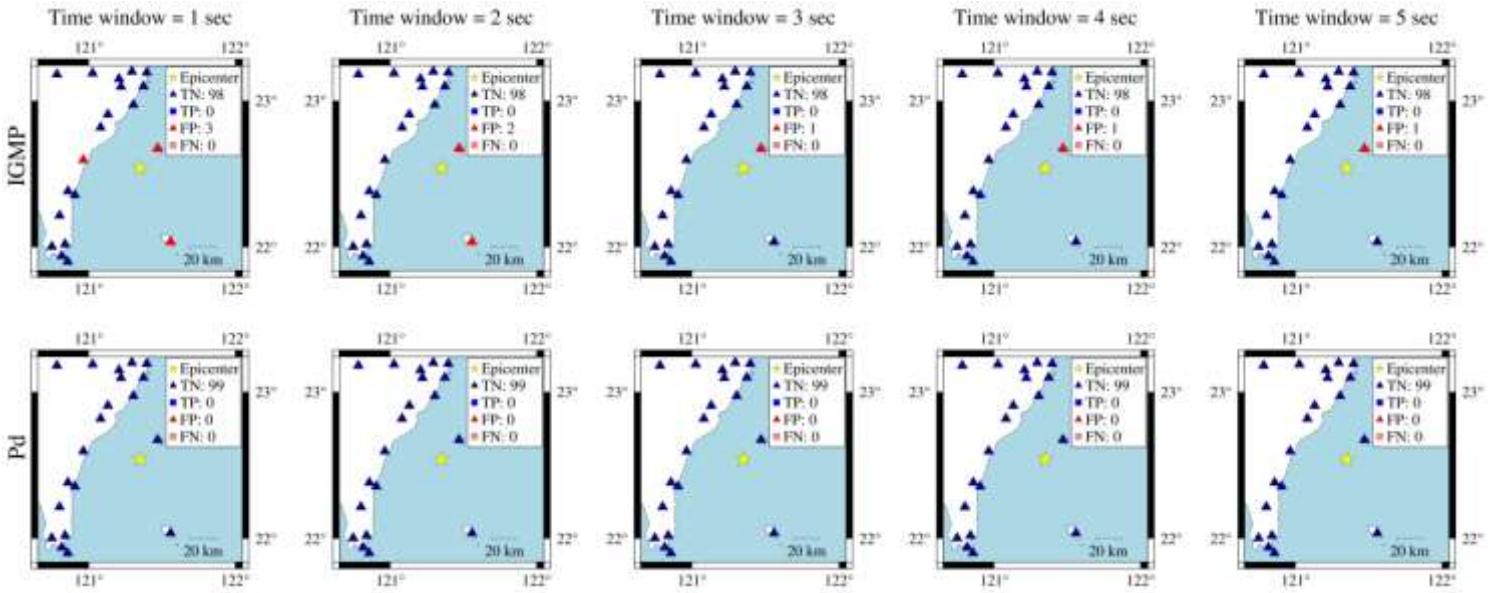

圖 17 臺東海外地震的模型預測結果

4.5 實際應用成果

4.6.1 地震預警系統

目前我們所採用臺大地質系吳逸民教授建立之地震觀測網，結合 Earthworm 的地震資料蒐集開源軟體，透過此系統，我們可以接收來自全臺超過 700 個測站的即時三軸波形資料，對其進行分析。此系統由兩種組件合成，一個名為 Ring，是一種共享記憶體，專門存放各種資料，如波形資料、被觸發到的測站、地震的預測結果等，是一個儲存空間；另一個組件是模組，透過讀取 Ring 中的資料以進行後續分析，將結果存至另一個 Ring 或是另行他用。圖 18 為該系統的簡易架構圖，透過 Palert2ew 模組可以將全臺灣超過 700 個測站的即時波形資料傳入 WAVE RING 中，再透過 Pick_eew 模組監測各測站的波形狀況，若

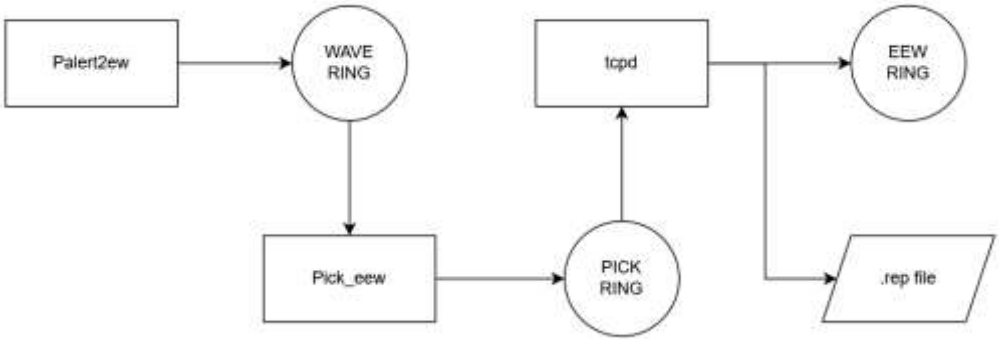

圖 19 地震預警系統 Earthworm 簡易架構圖，方形為模組，圓形為資料宁列，平行四邊形表示輸出檔案

任一個測站的資料超過一定閥值,便觸發該測站,將其資料放入 PICK RING 中,接著 tcpd 模組會記錄 PICK RING 中的資料，若 1 分鐘內有超過 4 個測站被觸發放到 PICK RING，則會判定有一個地震事件發生，在計算出地震的震央、規模、深度等資訊後，便會把結果存入 EEW RING，並產生一個以當下時間為檔名的 rep 檔，以供後續追蹤或寄送預警通知使用。

4.6.2 Palert 測站

目前全臺有超過 700 個測站，使用 Palert 感測器(如圖 20)。Palert 測站遍布於臺澎金馬各地中小學，可偵測地震波蒐集三軸的加速度資料，並將即時波形資料透過網路傳送至地震預警系統中以進行偵測及處理，這些測站組成一個觀測網，其分布如下圖 21。

圖 20 Palert 感測器

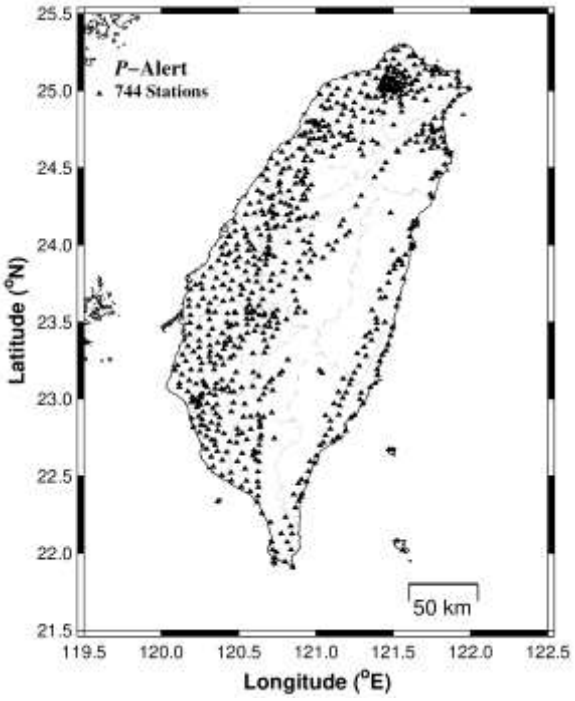

圖 21 測站分布位置

4.6.3 實驗模型實際應用於即時預警系統

在此實驗中，我們亦將上述模型結果應用至實際地震預警系統中，如圖 22 的架構圖所示，其中黃底為新增的模組，前段流程如 4.6.1 中所述，原始地震波會被 Palert2ew 送入 WAVE RING，並經由 Pick_eew 模組進行偵測，若有任一個測站偵

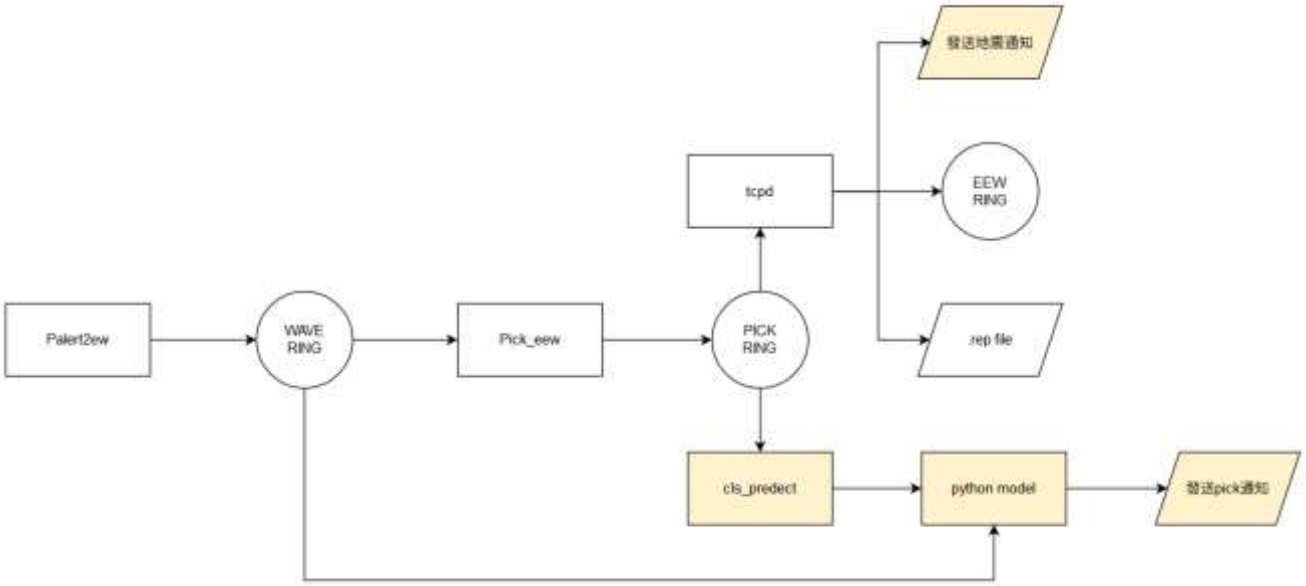

圖 22 地震預警系統架構圖 Earthworm 架構圖，黃底部分為新增區塊

測到地震波，便會將其資料送入共享記憶體 PICK RING 中，此時 cls_predict 模組會根據 PICK RING 中的資料觸發 python IGMP 模型，模型會至 WAVE RING 中抓取該測站的原始波形資料，針對該測站的波形進行預測，將結果透過 LINE 進行預警通知，如圖 23 (a) 所示，以達成現地型預警的目的。若一分鐘內有超過 4 個測站偵測到地震波，tcpd 模組便會啟動，判定為一個地震事件，在算出地震的震央、深度及規模後除了將結果寫入 EEW RING 並產生 rep 檔外，也會發送如圖 23 (b) 的 LINE 通知，告知地震的各項資訊並附上預測震源及測站圖，讓使用者可以即時收到預警通知，以及早應對地震波的到來。

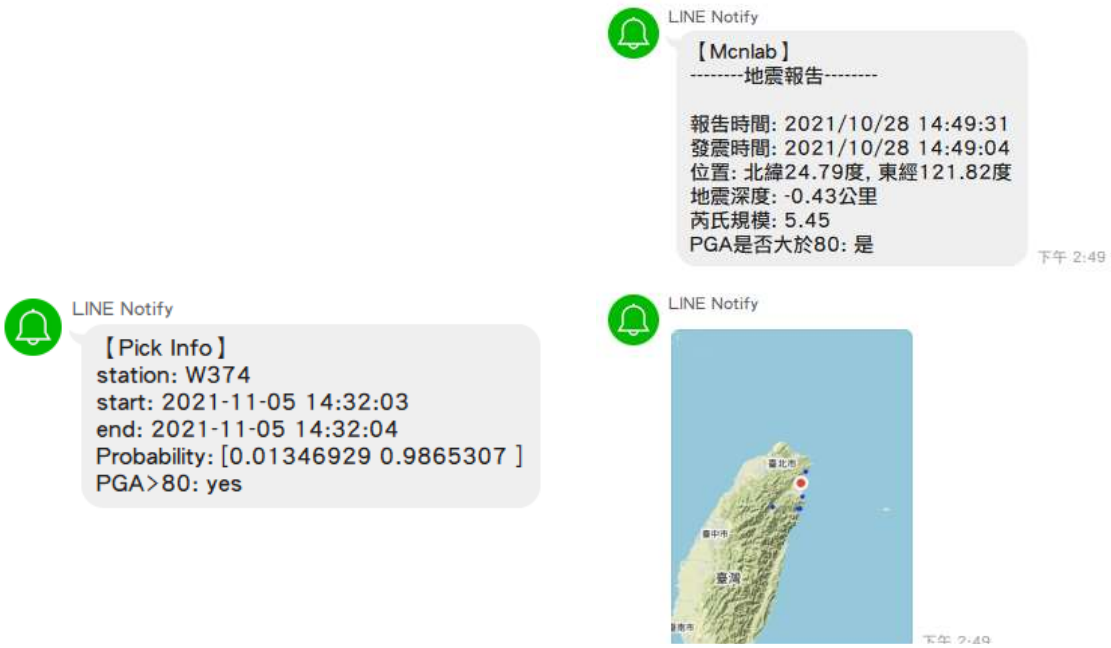

圖 23 (a) 測站被觸發時發送的預測通知 (b) 發生地震時所發送的預警通知

4.6 結論

本研究提出使用類神經網路的方法，利用 P 波到達後數秒的資料來預測震央附近測站的 PGA 是否大於(包含)80Gal。使用過去臺灣觀測網收集到的事件資料對模型進行訓練，透過真實事件做測試和使用 Pd 方法來做比較，評估本研究方法(IGMP)的成果。結果顯示 IGMP 有很高的 F1-score 和較長的平均 Leading time，代表其可靠度高和更多的反應時間。在震央分別位於島內和外海的兩個範例中，IGMP 也能精確的預測出震央附近是否有 PGA 高達 80Gal 的測站，如果有則可以立即對近震央區域發出警報，對於其他較遠的區域，也能夠發布預警，來增加反應時間。

5 類神經網路應用於地震波生成

5.1 簡介

類神經網路目前在各式各樣的領域上都有非常好的表現，其使用大量的資料做學習、擷取特徵，最後學會去解決特定的目標。而在地震領域上也已經有不少關於類神經網路的研究與應用，成果也顯示可以幫忙解決許多問題。由於使用類神經網路應用於地震等任務需要大量資料，地震震度高的與震度低的資料相比下來非常不平衡，會造成類神經網路無法順利學習。因此本研究為了平衡資料，以訓練對抗式生成網路來產生人工資料的方式當作資料擴充，目標是提高其他類神經網路的表現。

5.2 資料處理

本研究使用的資料集來自中央氣象局 CWB 觀測網中，時間從 2012/01/01 到 2021/10/7 的測站紀錄，包含加速度地震儀、寬頻速度地震儀、短周期速度地震儀，目的是作為生成資料的標準。另外還有來自 STandford Earthquake Dataset(STEAD)資料集中隨機選擇 20000 個規模大於 3 的地震資料和 20000 個雜訊資料，目的是用於訓練模型。為了能學習高震度的資料特徵，我們只使用規模大於(包含)3 的地震事件資料

所有地震資料會先經過 Max-Min Normalize 正規化後再放入模型中進行訓練與測試，產生出來的資料會依照輸入地震波型的振幅還原回正常大小，作為新產生出來的地震波資料。

5.3 模型架構

本論文模型參考自論文“Seismic Data Augmentation Based on Conditional Generative Adversarial Networks”，其架構如圖 24 所示。主要有生成器(Generator)、判別器(Critic)、特徵擷取器(Feature Extractor)三個部分。其中生成器的目標是要產生出能騙過判別器的地震訊號，而判別器目標是要能分別出輸入資料是生成器所產生的還是真實的地震資料，這兩者會透過不斷的競爭、改進自身，最後生成器會有能力產生出非常相似於真實地震的資料。而特徵擷取器的目標在於幫助生成器學習真實地震的特徵，進而使產生出來的資料變得更像真實資料。

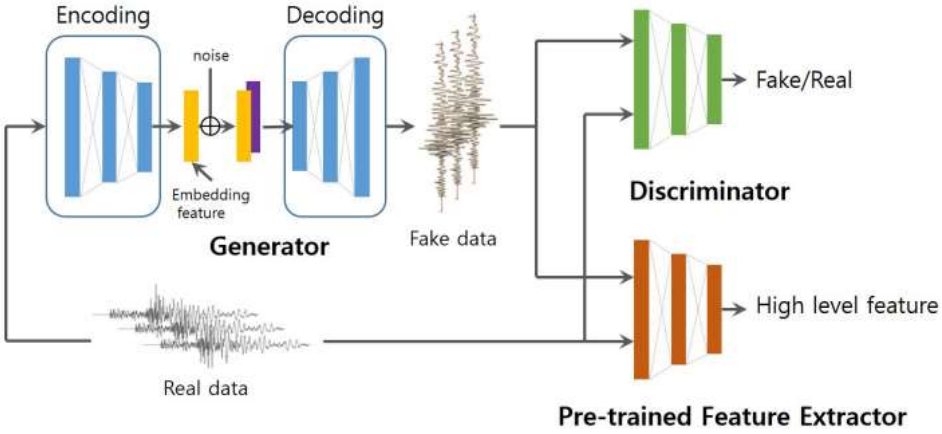

生成器使用 encode-decoder 架構，如圖 25 所示，encoder 負責把輸入地震資料

圖 24 對抗式生成網路架構

壓縮並提取特徵，接者加上雜訊使特徵資料產生變化，最後再由 decoder 重組壓縮的特徵資料，形成新的地震資料。為了防止資料的損失，會將 encoder 過程中的特徵資料傳到 decoder 過程中幫助產生新的地震資料。Encoder 中包含五個區塊(Down Block)，每一個區塊由一個一維卷積、Batch Normalization 和整流線性單位函數（Rectified Linear Unit, ReLU）組成，分別的作用為特徵提取、歸一化資料與激勵函數。一維卷積的 kernel size 分別為 5、5、5、3、3，stride 都為 2，channel 分別為 16、32、64、128、128。Decoder 包含四個區塊(Up Block)，每一個區塊由一個一維卷積、Batch Normalization、ReLU、Dropout、SubPixel、Concat 組成，其中 Dropout 可以讓模型不要過度學習訓練集中的資料，而使得跟真實情況不符，SubPixel 是一個可以在反卷積時，解決特徵資料不均勻重疊的問題，Concat 則是用於將 encoder 傳送到 decoder 的資料做統合，以避免資料損失。一維卷積的 kernel size 分別為 3、5、5、5，stride 都為 1，channel 分別為 128、64、32、16。最後再經過一個 kernel size 為 5、stride 為 1、channel 為 6 的一維卷積和 SubPixel 幫助將特徵統合、重組為一個新的地震資料。

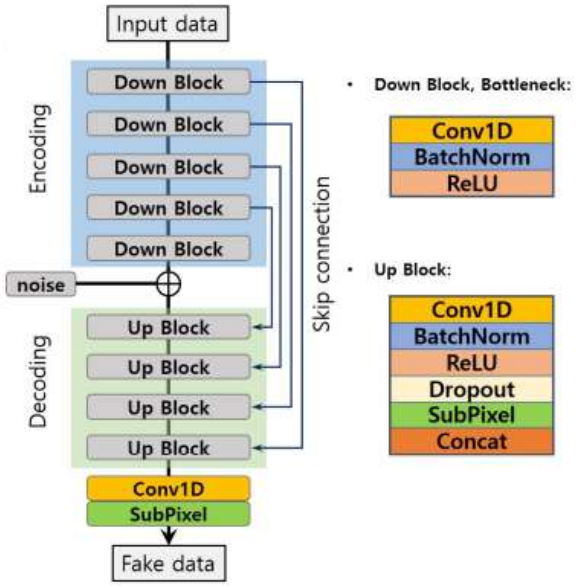

圖 25 生成器網路架構

判別器由六個區塊(CNN Block)、Flatten、Dense 和一個 Sigmoid 函式組成，如圖 26 所示，每個區塊都由每一個區塊由一個一維卷積、Batch Normalization、Leaky ReLU 做為激勵函式組成。一維卷積的 kernel size 都為 10，stride 都為 2，channel 都為 64。而 Flatten 的功用是將所有特徵資料轉換成一向量資料，經過 Dense 統合出判別結果資料，最後 Sigmoid 函式會將其轉換成介於[0,1]之間的機率值，來代表輸入的波型資料為真的地震的機率。

特徵擷取器是一個是先訓練好的模型，如圖 27 所示，整體如判別器類似，

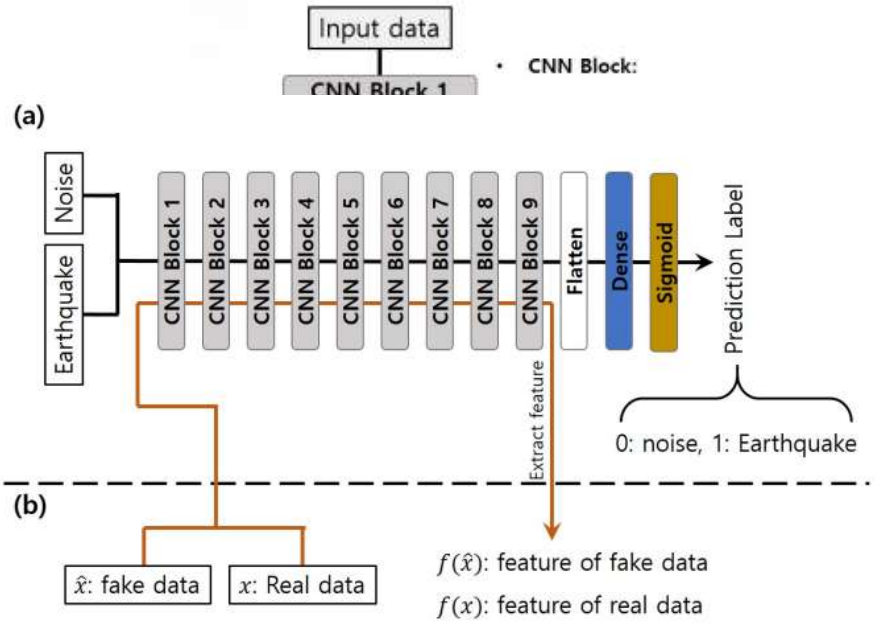

圖 27 特徵擷取器網路架構

但其包含九個與判別器相同的區塊，而這九個區塊可以做為特徵擷取器來用。

5.4 訓練過程

在模型訓練過程中，生成器、判別器、特徵擷取器所使用的優化器都是 Adam、學習率為10^{-5}、batch size 為 64。首先，特徵擷取器會先使用地震資料與雜訊資料做訓練，經過 100 輪的訓練後，再將其前面九個區塊獨立出來，加入到接下來生成器與判別器的訓練過程中，幫助生成器進一步學習地震資料的特徵。接者，生成器和判別器會開始交互訓練，生成器會將產生出來的地震資料與真實地震資料輸入到判別器中，讓其學習分辨真假，判別器和特徵擷取器則會分別把分辨結果與真實資料與生成資料之間的特徵差別回饋給生成器做改進、學習產生出更像真實地震的資料，經過 1000 輪交互訓練後就會停止訓練。

5.5 具體表現

5.5.1 生成資料成果

本實驗使用的資料集來自中央氣象局 CWB 觀測網中，時間從 2012/01/01 到 2021/10/7 的測站紀錄，包含加速度地震儀、寬頻速度地震儀、短周期速度地震儀。只使用規模大於(包含)3 的地震事件資料。

如圖 28 圖 29 所示，左邊是真正的地震資料，右邊是產生出來的地震資料，可以看出產生出來的地震資料非常相似於真正的地震資料。

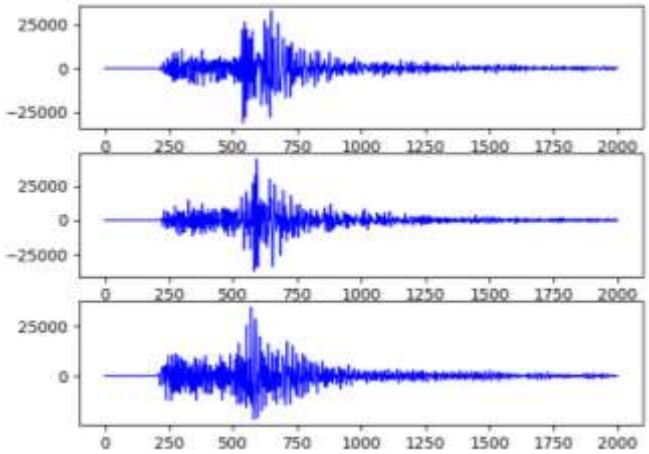

圖 28 真正的地震資料

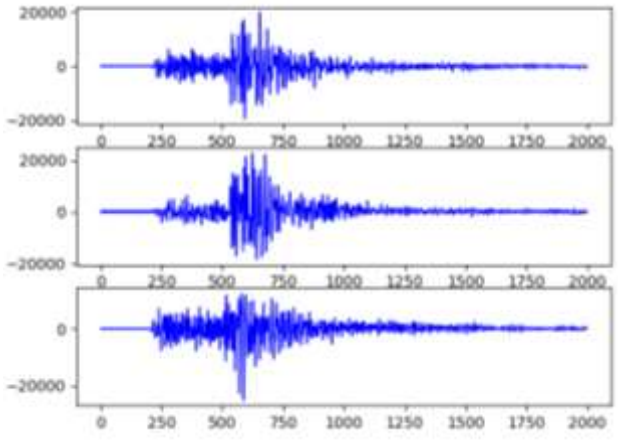

圖 29 生成的地震資料

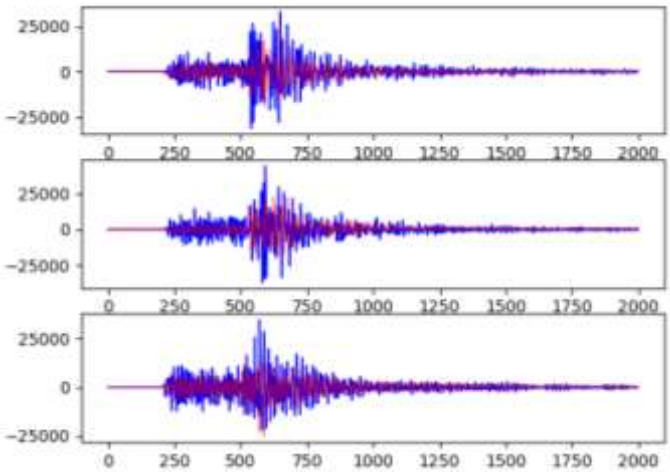

圖 30 真實地震訊號與生成地震資料差別

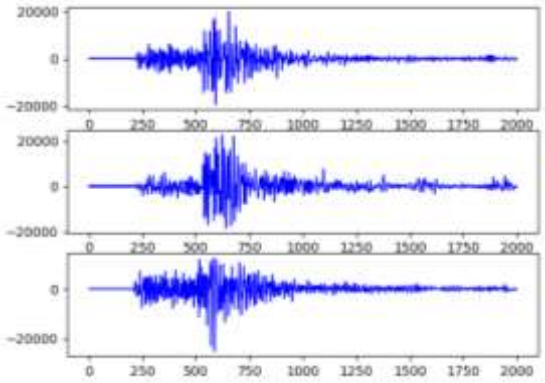

圖 31 平均值 0、標準差 5 的生成資料

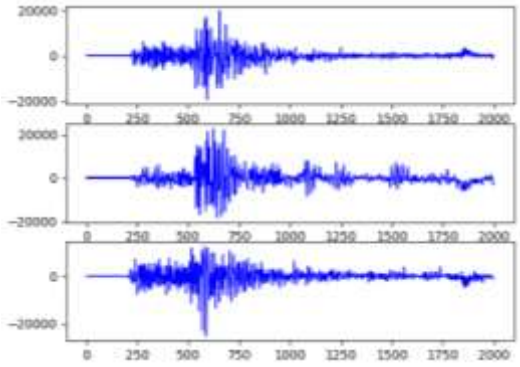

圖 32 平均值 5、標準差 20 的生成資料

兩者在架構上大致是相同的，而在震幅上則有些差別，如圖 30 所示，藍色代表真實資料，紅色代表生成資料。

為了補足更多的高震度地震資料，我們調整了輸入雜訊的平均值與標準差，由一個資料產生了更多不同的生成資料，如圖 31 圖 32 所示，左邊是平均值為 0、標準差為 5 的生成地震資料，右邊是平均值為 5、標準差為 20 的生成地震資料。

而生成地震資料之間的架構大致上相同，震幅上則有些差別，如圖 33 圖 34 所示，兩圖中藍色的代表平均值為 0、標準差為 1 的生成地震資料，左邊其與平均值為 0、標準差為 5 之生成地震資料的比較，右邊其與平均值為 5、標準差為 20 之生成地震資料的比較。

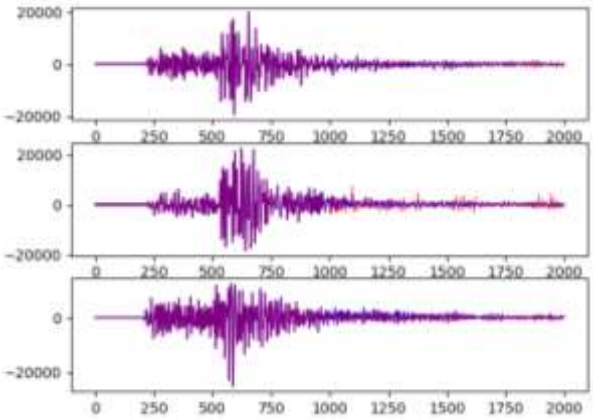

圖 33 生成地震資料差異比較(1)

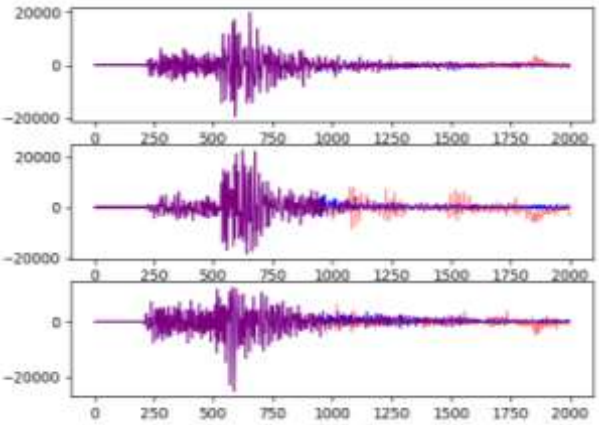

圖 34 生成地震資料差異比較(2)

5.5.2 生成資料應用於震度分類任務之成果

在地震震度分類任務上，因為高震度的資料會遠少於低震度的資料，造成訓練資料的不平衡，導致類神經網路模型對於高震度資料不敏感，從而導致預測結果錯誤。因此如果使用本研究所產生出來的地震資料，補足過度缺少的高震度資料，就能適當緩解資料不平衡的問題。

用於預測的資料為 P 波到時後 1、2、3、4、5 秒的加速度資料，輸出則為所預測的震度，分別為 0、1、2、3、4、5.1、5.5、6.1、6.5、7，共十個震度分級。本研究使用的資料集來自中央氣象局 CWB 觀測網中，時間從 2014/01/01 到 2020/10/7 的測站紀錄，包含加速度地震儀、寬頻速度地震儀、短周期速度地震儀，另外還有來自日本 K-NET 的測站紀錄。將地震資料經過統合及挑選後分為訓練集和測試集，其震度分佈如圖 35 圖 36 顯示。

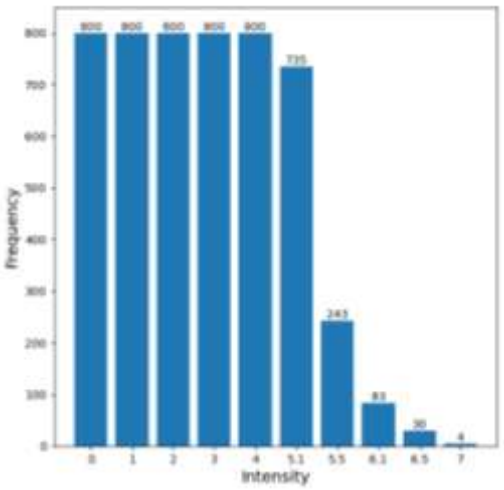

圖 35 訓練集之震度分佈

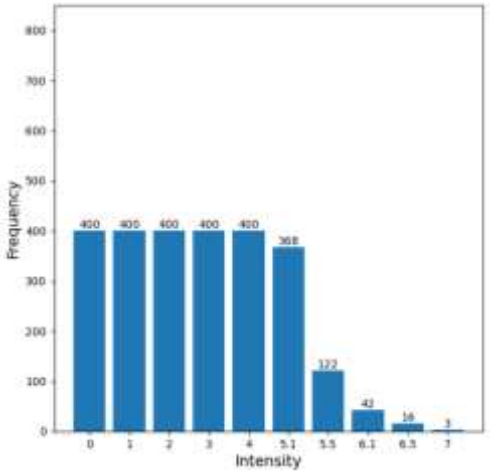

圖 36 測試集之震度分佈

為了平衡資料，我們將生成的地震資料加到訓練資料中形成新的訓練資料，其震度分部如圖 37 所示。不完全補充各震度資料到相同數量的原因是不希望模型過度著重於分類生成資料，而忽略真正的地震資料，導致真實應用時反而成效變差。

模型所使用的是以兩個 Transformer 和一個 fully connection 所組成的分類器。Transformer 可以幫助注意輸入 P 波資料中重要的特徵，而 fully connection 則會把重要的資料統合並進行分類，最終輸出分類結果。

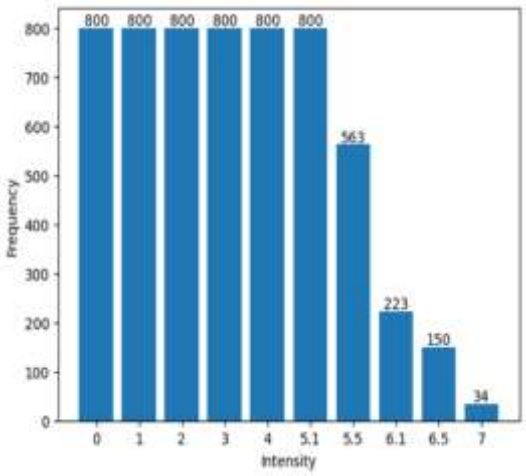

圖 37 訓練集之震度分佈(加入生成資料後)

如圖 38 所示，分別以 P 波到時後 1、2、3、4、5 秒訓練集訓練，以測試集測試後各地震震度分類的精確度，紅線所代表的是原始的資料集(沒有加入生成地震資料)，藍線所代表的是資料擴充後的資料集(有加入生成地震資料)。可以看出只有在某些部分有小幅度提升，整體表現並沒有太大的提升。造成此狀況的可能原因為生成模型能力還不足夠、資料選擇與處理不夠精確等，這些都會做為未來研究改進的方向。

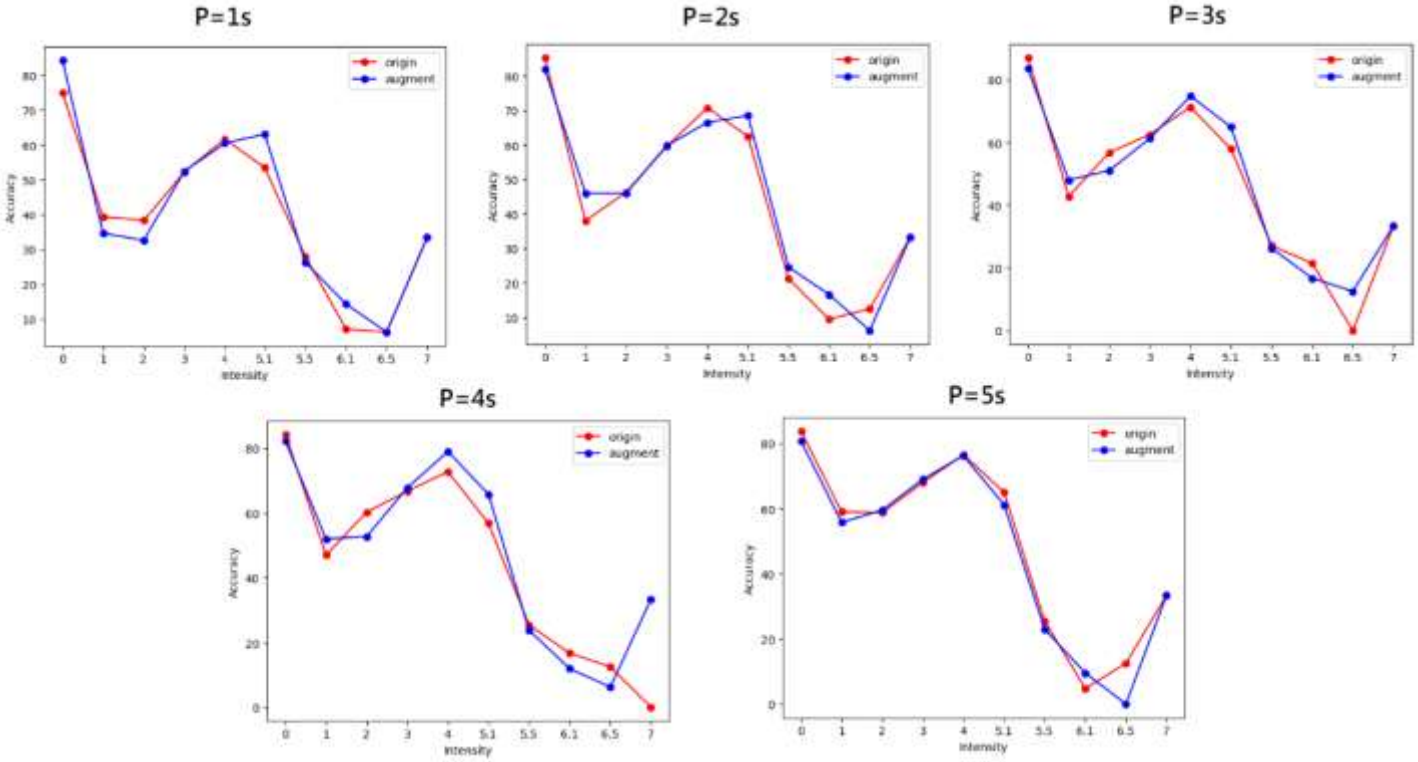

圖 38 各 P 波長度輸入之震度預測結果

5.6 結論

本研究提出使用類神經網路中的對抗式生成網路架構，產生出非常相似於真實地震的資料，以解決高震度資料遠少於低震度資料所造成的資料不平衡。使用過去臺灣觀測網收集到的事件資料，產生出新的地震資料並用來擴充模型的訓練集資料。結果以視覺上，產生出了非常類似於真實地震事件的資料，包含 P 波和 S 波等重要特徵，但缺點是產生出來的結果太過相似於原本資料，使得能產生出來的變化不多、資料少。另外，還利用產生的資料對訓練集做資料擴充，增加高震度資料來平衡各震度分類的數量差別，用以訓練震度分類模型。實驗結果只有部分分類有小幅度上升，整體上仍沒有太大進步。未來會再針對這些點進行研究解決方法、修改模型架構、調整參數或權重、整理品質更好的資料集，以產生出更好的結果。